

III. Ultrasound and Biomechanics

1. Ultrasound

Scanning acoustic microscopy of human septal cartilage

S. Burkert^{a,*}, S. Liebhold^a, E.J. Haberland^a, A. Klemenz^c, J. Brandt^b and M. Bloching^a

^aDepartment of Otolaryngology, Head and Neck Surgery, ^bDepartment of Orthopaedics, ^cDepartment of Anatomy and Cell Biology, Martin-Luther-University Halle-Wittenberg, Magdeburger Str. 12, 06097 Halle, Germany

Introduction: The properties of cartilage depend on its microstructure. In order to understand the behaviour of nasal cartilage, it is therefore important to observe and characterize the complex structure. There is now a wealth of powerful techniques available and had been used for examination of cartilage, including optical microscopy, electron microscopy, etc. Scanning acoustic microscopy (SAM) is used for very high resolution acoustic imaging. Spatial resolution is comparable to light microscopy, but the nature of confocal image generation with acoustic waves provides additional surface and subsurface information [1,2].

Methods: Human nasal septal cartilage samples were prepared for ultrasound and microscopic analyses. The samples were initially incubated under physiological condition in cell culture medium (Gey's solution[®]) with antibiotics. To achieve a smooth surface the cartilage were cut with a microtome (Jung Biocut 2035, Leica). After ultrasound data acquisition the septal cartilage were fixed in formalin solution and conventionally embedded in wax. Sagittal contiguous section (5–10 μm thick) were performed. Then the sections were stained with hemotoxillin-eosin (HE) and alcian. The used scanning acoustic microscope operates in reflection mode and can be regarded as a surface imaging technique, dependent only upon changes in the elastic properties across the surface of a sample. The image is built up by mechanical scanning of a focused beam of ultrasound across the surface of bone, with the acoustic signal returned from the specimen displayed on a monitor. The ultrasound is emitted by a transducer. After interacting with the cartilage, the reflected waves return to the transducer via the lens. The lens is coupled to the specimen by water. A set of C-scan images with a successively decreasing distance between the lens and the sample surface is acquired. From the 3D data set both the topography and a topographically corrected map of reflectivity can be reconstructed. The latter can be used for a quantitative characterization of mechanical properties. The technique compensates for alterations in the image contrast other than those caused by varying mechanical material properties to a certain extend.

Conclusion: High frequency ultrasound provides a potential method for the measurement of elasto-mechanical properties of nasal septal cartilage. Changes in echo intensity of the cartilage surface observed in scanning acoustic microscopy at a frequency of 400 MHz result from different tissue constitution and properties. Further work is conducted to optimize the surface preparation.

*Tel.: +49 345 5571667; Fax: +49 345 557 4161; E-mail: silke.burkert@medizin.uni-halle.de.

References

- [1] A. Klemenz, C. Schwinger, J. Brandt and J. Kressler, Investigation of elasto-mechanical properties of alginate microcapsules by scanning acoustic microscopy, *J Biomed Mater Res* **65A**(2) (1 May 2003), 237–243.
- [2] S. Burkert, E.J. Haberland, K. Raum, A. Klemenz, J. Brandt and A. Berghaus, Tissue characterization of human auditory ossicles by scanning acoustic microscopy, *IEEE Symp* (2002), 1273–1276.

Resolution improved parameter estimation based on raw data of spatial compound scans

K.-V. Jenderka

PTB Braunschweig and Q-BAM Group Halle, Germany

Tel.: +49 531 592 1432; Fax: +49 531 592 1405; E-mail: klaus-vitold.jenderka@ptb.de

Introduction: Different methods for determination of quantitative acoustical tissue parameters based on the analysis of B-mode image data, raw data or acquired rf-echo data are well established. Ultrasound rf data contain most information, especially about the frequency content of the back scattered echoes. Unfortunately up to now rf-data and system settings are only available in some configurations of clinical scanners. Furthermore usual procedures for parameter estimation, e.g. attenuation using the multi-narrow-band method, require relative large roi (region of interest) with a minimum size in scan direction of 1 cm to obtain reliable results.

Methods: The raw-data of complete spatial compound imaging scans (SonoCT[®]) of a clinical ultrasound device (HDI 5000, Philips Medical, Bothell) are used for parameter estimation. In these imaging technique scans obtained with beams steered in different directions merged to one image (Fig. 1).

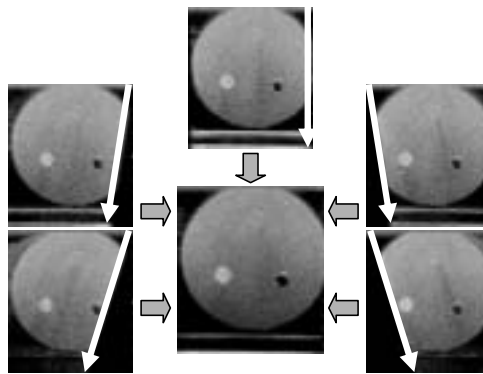


Fig. 1. Principle of spatial compound imaging. In example the beam is steered in 5 steps from -17° to $+17^\circ$. Note the reduced shadowing artifacts and speckle.

Using the raw data sets of all scanned angles the attenuation estimates were determined in uniform, overlapping roi. Assuming this attenuation data as projections of the local attenuation distribution obtained from different directions, the local attenuation values are found by application of the inverse Radon transformation (Fig. 2). In any case, routines for the correction of time gain compensation and sound field characteristic were applied.

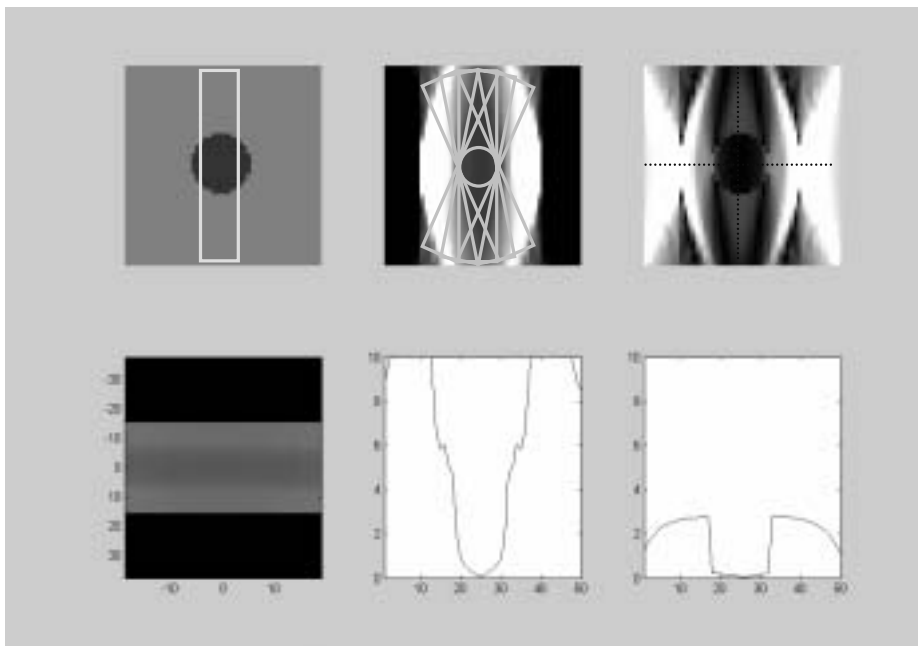


Fig. 2. Simulation results for circular inclusion. Top row: original attenuation map, reconstructed attenuation map (5 angles in steps of 8.5°), difference map between original and reconstruction. Bottom row: projections of the original attenuation map (radon transformation), attenuation differences along central horizontal and central vertical line.

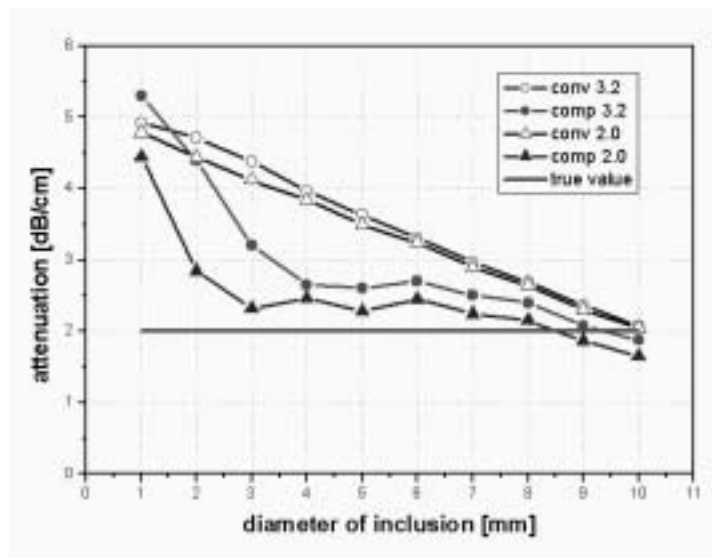


Fig. 3. Comparison between conventional (conv) and compound (comp) method for estimation of attenuation in small inclusions (3.2 mm and 2.0 mm).

Results: A comparison between conventional multi narrow band method and the compound technique was carried out by simulation of different sized inclusions (Fig. 3). Down to inclusion diameters of approximately 3 mm the simulation results show much better estimates of the attenuation value.

Furthermore tissue mimicking phantoms were investigated in conventional imaging and spatial compound imaging mode. The effective roi size was reduced down to 3 mm. The result of 64 single estimates in a square roi of 18 mm came to $\alpha = 4.22 \pm 0.97$ dB/cm (at 6.5 MHz). The estimated mean value of the attenuation parameter showed a good agreement with the acoustical properties of the phantom obtained in transmission mode.

Conclusions: The analysis of spatial compound imaging raw data provides local attenuation coefficients in the mid-band range of the transducer leading to local data parameter images of quantitative acoustic tissue parameters. In combination with conventional b-mode, parameter imaging has the potential to support the diagnosis of pathological changes in tissues.

Imaging of ultrasound attenuation coefficient

R. Jířík^a, T. Taxt^b and J. Jan^a

^a*Department of Biomedical Engineering, Brno University of Technology, Brno, Czech Republic
Tel.: +420 541 149 557; Fax: +420 541 149 542; E-mail: jirik@feec.vutbr.cz*

^b*Department of Physiology, University of Bergen, Bergen, Norway*

Introduction: The paper studies imaging of tissue-specific ultrasound attenuation. Ultrasound attenuation parameters are closely related to the type and the pathological state of the tissue. Therefore, the estimated attenuation parameters can be used as a feature in quantitative tissue characterization [2,3]. Ultrasound attenuation is also an important factor affecting spatial resolution of ultrasound images since the higher ultrasonic frequencies are attenuated more than the lower ones. Knowing the attenuation as a function of frequency and depth allows estimation of the depth-dependent point spread function component caused by attenuation. This component can be used to improve the spatial resolution of the ultrasound image through deconvolution [2].

This paper introduces a method, for tracking the attenuation coefficient in B-mode ultrasonic images on a pixel-by-pixel basis. The resulting parametric images show, for each pixel, the mean attenuation coefficient between the probe and a given pixel position, further referred to as the cumulative attenuation coefficient.

Method: The estimation of the cumulative attenuation coefficient is based on the following 1-D physical model of ultrasound radiofrequency signal $S(\omega, d)$ in the Fourier domain:

$$S(\omega, d) = c(d)G(\omega)e^{-2\bar{\beta}d|\frac{\omega}{2\pi}|+i\phi(\omega)}R(\omega, d), \quad (1)$$

where d is depth, $c(d)$ is a depth dependent factor accounting for phenomena affecting all frequency components to the same extent (frequency independent attenuation, time gain compensation), $G(\omega)$ is a Gaussian-shaped spectrum, centered at the mean frequency of the probe, modeling the electroacoustical round-trip transfer function of the transducer. $R(\omega, d)$ is the tissue function characterising the diffuse scatterers and specular reflectors at the depth d . The exponential term represents the attenuation transfer function [2], with the phase response $\phi(\omega)$ and $\bar{\beta}$ denoting the cumulative attenuation coefficient.

A-scan radiofrequency signals are first divided into short (~ 4 mm) overlapping segments. Each segment is then transformed from the time domain to the log-spectrum domain. The cumulative attenuation coefficient is estimated for each segment by means of the least-mean-squares approximation of

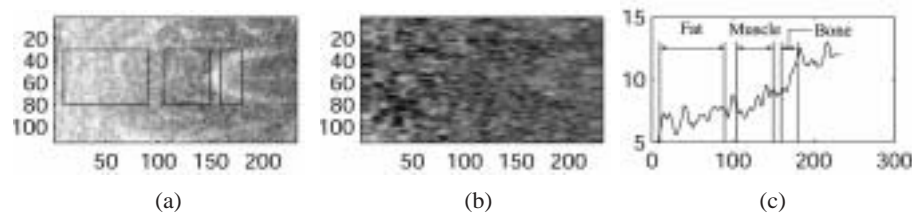


Fig. 1. Estimation of attenuation parameters on image of thigh. (a) Envelope image – the beams are oriented horizontally with the depth increasing from left to right. (b) Cumulative attenuation coefficient image. (c) Estimation of the local attenuation coefficient.

the segment log-spectrum using its physical model, derived from Eq. (1). The parametric image is then formed from estimates of the cumulative attenuation coefficient in each segment of each beam.

It can be shown that a local tissue-specific attenuation coefficient can be estimated from the modified images of the cumulative attenuation coefficient, where each pixel is multiplied by its corresponding depth. This is done by linear regression applied to regions of the modified images within a homogeneous tissue.

Results: The proposed method was tested on images of a tissue-mimicking phantom Gammex 403GS, and on clinical images of liver and thigh. The resulting images of the cumulative attenuation coefficient show some of the tissue structures (example image – Fig. 1(b)).

In selected regions of these images (the regions depicted in the input envelope image – Fig. 1(a)), the local tissue-specific attenuation coefficient was estimated. In Fig. 1(c), the plots of averaged beams of the modified parametric images (the cumulative attenuation coefficient multiplied by depth) are shown. Only the beams crossing the used regions are considered in averaging. The vertical lines in the plot of Fig. 1(c) denote the borders of the regions in the axial direction. In the ideal case, the plot would be piece-wise linear with different slopes in different homogenous regions, corresponding to the local attenuation coefficients.

The estimates of the local attenuation coefficient were compared with reference values. For phantom images, this reference value was given by the specifications of the used phantom. For the clinical images of liver and thigh, the reference values were taken from literature [1]. The estimated local attenuation coefficients were mostly in accordance with the reference values.

Conclusion: The paper presents a new method, which could have the potential to show tissue-specific ultrasound attenuation properties or to be the preliminary step in deconvolution of ultrasound images. The resulting parametric images are, however, still fairly noisy, probably due to the inaccuracy of the spectrum estimation from short segments and due to the deviations of the used model from the real radiofrequency signal. These problems are the subject of our further research.

Acknowledgement: The project has been supported by the Research Council of Norway, by the grant no. 102/02/0890 of the Grant Agency of the Czech Republic and by the grant no. 1K03017 of the Czech Ministry of Education, Youth and Sports.

References

- [1] B. Angelsen, *Ultrasound Imaging – Waves, Signals, and Signal Processing*, Emantec AS, 2000.
- [2] B.J. Oosterveld, J.M. Thijssen, P.C. Hartman, R.L. Romijn and G.J.E. Rosenbusch, Ultrasound attenuation and texture analysis of diffuse liver disease: Methods and preliminary results, *Phys. Med. Biol.* **8** (1991), 1039–1064.
- [3] L.S. Wilson, D.E. Robinson and B.D. Doust, Frequency domain processing for ultrasonic attenuation measurement in liver, *Ultrasonic Imaging* **3** (1984), 278–292.

Ultrasound Characterization of Soft and Hard Biological Tissues

Quantitative SAM investigation of changes in cartilage and subchondral bone due to primary arthrosis

S. Leicht, K. Raum and J. Brandt

Department of Orthopedics, Martin Luther University of Halle-Wittenberg, Q-BAM Group, Halle, Germany

Tel.: +49 345 5571317; Fax: +49 345 5574899; E-mail: sonja.leicht@student.uni-halle.de

Introduction

The study aims at showing changes of articular cartilage and subchondral bone structures due to primary arthrosis in human tibia plateaus using a 50 MHz–200 MHz scanning acoustic microscope (SAM).

Methods

A custom scanning acoustic microscope (Q-BAM, Halle, Germany) was used. It consists of a 3 axis high precision scanning stage, a 200 MHz pulser/receiver (Panametrics 5900PR) and a 500 MS/s A/D-card (Gage 8500). All components are controlled by custom software. A spherically focused 50 MHz transducer (V605: Valpey Fisher, Hopkinton, USA) provided a spatial resolution of 23 microns.

Measurements were performed on 23 human tibia plateau samples taken from endoprothetic surgery. During preparation and measurements the samples were kept in hyperosmolar NaCl solution (3 molar) to prevent extensive cartilage swelling. The samples were cut sagittally in 3 parts on both the medial and the lateral site of the plateau. The 6 parts of each sample were attached to slides with the cartilage/bone interface upside. After freezing the samples in liquid nitrogen a flat surface was prepared by an ultra precision milling machine. After thawing the samples were explored in degassed hyperosmolar NaCl solution at 50 MHz in a temperature controlled tank at 25°C.

Each sample was measured twice with calibrated receiver settings optimized for greatly different impedance values in cartilage and bone.

Results

The mean impedance values in cartilage and bone were 2.1 Mrayl and 6.3 Mrayl.

For cartilage and bone the impedance was evaluated as a function of the distance to the interface (arrow in Fig. 1(a)).

Cartilage

In most samples substructures, indicated by different impedance values, were found within the cartilage. Generally values were higher close to the bone interface and decreased continuously up to the surface (Fig. 1(b)). Usually two or three layers with different impedance values were detected (areas between bars in Fig. 1(b)). In some samples in addition to the three layers a slight increase of impedance was seen between the middle and surface layer.

As an additional parameter we used cartilage swelling which generally shows three layers of different swelling behavior within the cartilage. Cartilage close to the bone hardly changes after preparation, the

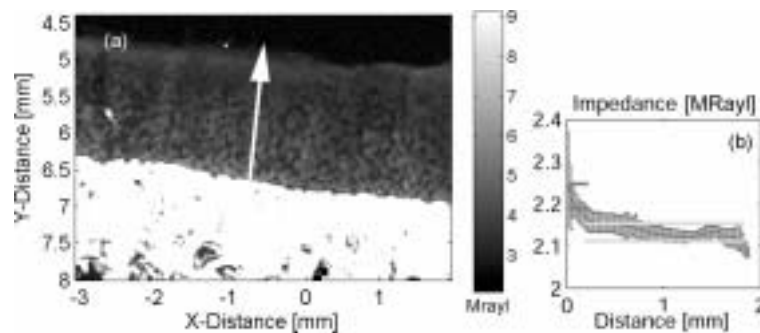


Fig. 1. Acoustic impedance image (a) of cartilage with a lower grade of arthrosis. A layered structure with different impedance values is visible. By rotating and reshaping the image the impedance values can be shown as a function of distance to the cartilage-bone boundary (b) (0 = cartilage/bone interface). The Impedances of the deep layer (between dark gray bars) and the middle layer (between lighter gray bars) are significantly different; a slight increase of impedance in the subsurface zone at about 1.8 mm from interface is detectable.

middle layer shrinks and the surface layer slightly swells (absolute height difference between $20\ \mu\text{m}$ and $80\ \mu\text{m}$) which corresponds to the anatomic and biochemical composition of human articular cartilage. Some samples showed an uneven undulating surface with height differences of $120\ \mu\text{m}$ compared to the bone surface.

The comparison with histological procedures of the investigated samples is under way. In Tenascin stained samples detection and grading of arthrotic destruction seems to be possible and comparable to the detected grade found with SAM. Other staining and a statistical evaluation will follow.

Bone

In subchondral bone a significant increase of the impedance compared to the mean values was observed close to the interface in nearly 60% (54/91) of the samples.

Discussion

Cartilage

Our preliminary results suggest that structural damages are seen both with SAM and histology (fissures, surface roughening). Lower grades of osteoarthritis exhibit a 3- or 4-layered structure (Fig. 1(a)). In most cases the deepest and middle layer indicate significant different impedance values (Fig. 1(b)). The fourth layer seen just below the surface in lower grades might be due to reparation processes. Similar observations were made in Backscatter-microscopy by Saied et al. in experimental induced osteoarthritis [1,2] and during maturation in rat cartilage [3].

Moreover in lower grades shrinking of the middle layer occurs. Higher grades show a loss of the layer structure and a rather uneven surface with large height differences. This topography might be due to the amount of water uptake and the following preparation process. In order to prepare a flat surface on the soft cartilage the tissue has to be frozen in liquid nitrogen. Freezing causes a volume increase, which is dependent on the water content. The variable distribution of water in cartilage results in an inhomogeneous shrinking after thawing. In lower grade arthrosis the highest shrinking is in the middle layer, which is believed to have the highest water content [4]. In higher grades the layered structure is diminished. Therefore the characteristic shrinking pattern is less pronounced.

Bone

It is hypothesized that the impedance increase close to the bone cartilage boundary is an indicator for subchondral sclerosis. The latter is a common parameter for the clinical diagnosis of arthrosis and it is usually detected by X-Ray as areas of higher mineralisation.

Conclusions

With the proposed technique the investigation of native cartilage and bone samples is possible. We were able to detect even early osteoarthrotic changes both in structure and elastic properties with high frequency ultrasound.

It is expected that further investigations will improve our understanding of early changes during the pathogenesis of osteoarthrosis.

In prospect the results will be compared with non-arthrotic samples. Additional histological analysis as well as a full statistical evaluation will be performed.

Acknowledgments

This work was supported in part by the PROCOPE program # D/0122910.

References

- [1] A. Saied, P. Laugier and D. Chevrier, Experimental osteoarthrotic articular cartilage: *In vitro* visualisation of lesions and three-dimensional surface reconstruction using 50 MHz ultrasound microscope. 1475–1478. 1994. Proceedings Of The IEEE Ultrasonics Symposium. Ref Type: Conference Proceeding.
- [2] A. Saied, E. Cherin and H. Gaucher et al., Assessment of articular cartilage and subchondral bone: subtle and progressive changes in experimental osteoarthritis using 50 MHz echography *in vitro*, *J Bone Miner Res* **12**(9) (1997), 1378–1386.
- [3] E. Cherin, A. Saied and B. Pellaumail et al., Assessment of rat articular cartilage maturation using 50-MHz quantitative ultrasonography, *Osteoarthritis Cartilage* **9**(2) (2001), 178–186.
- [4] D.A. Narmoneva, J.Y. Wang and L.A. Setton, Nonuniform swelling-induced residual strains in articular cartilage, *J Biomech* **32**(4) (1999), 401–408.

Ultrasound Characterization of Soft and Hard Biological Tissues

Frequency dependence of the anisotropic impedance estimation in cortical bone

J. Reißhauer, K. Raum and J. Brandt

Department of Orthopedics, Martin Luther University of Halle-Wittenberg, Q-BAM Group, Halle, Germany

Tel.: +49 345 5571317; Fax: +49 345 5574899; E-mail janush.r@web.de

Introduction

Low frequency ultrasound has been extensively used for the characterization of the macroscopic elastic properties [1–6]. By increasing the frequency up to the gigahertz range it is possible to investigate the mesoscopic and the microscopic levels of structural organization [8–11]. Sound velocity and impedance values obtained at different frequencies suggest dispersion in bone [7–11]. In this study acoustic impedance distributions obtained with three focused transducers were compared. This allowed the additional consideration of morphological parameters in the investigation.

Materials and Methods

Samples

A variety of homogenous materials served as references for impedance calibration. Speed of sound and mass density of these materials were determined by a low frequency substitution method and by Archimedes' principle, respectively. Proximal cortical bone sections were obtained from human cadaver femora. After dehydration the specimen were embedded in PMMA. After cutting the sample perpendicular to the femoral long axis the surface was ground and polished.

Experimental setup

A custom scanning acoustic microscope (Q-BAM, Halle, Germany) was used. All components are controlled by a custom software. A set of spherically focused transducers provided a spatial resolution in the range from 150 down to about 20 microns. The samples were completely immersed in a temperature controlled tank filled with in distilled, degassed water at 25°C. C-scans were acquired, whereas for each scanned point the entire pulse echo signal was stored.

Impedance calibration and evaluation

For all reference materials the pulse echo signal was measured as a function of the sample-transducer distance. The band pass filtered, Hilbert-transformed confocal echo amplitudes were used for the impedance calibration. From the characteristic $V(z)$ curve of each transducer time-of-flight dependent defocus corrections were estimated.

The same processing was applied to the C-scan data. After defocus correction the echo amplitudes were converted into values of the acoustic impedance. Histogram evaluations were performed on identical stripes of 1 mm width for each frequency. Regions filled with the embedding material were excluded from the evaluation using a 4 Mrayl threshold mask. The histograms were normalized in order to compensate for different amounts of data for the individual scans.

Results

At 25 MHz the Haversian channels are not completely resolved, whereas at the higher frequencies the channels as well as the osteon boundaries can be distinguished.

The young samples have a larger number of osteons with a relatively small channel diameter ($< 50 \mu\text{m}$) compared with the senium samples, who have less osteons, but large channel diameter ($> 100 \mu\text{m}$).

After merging the histograms into the three frequency groups an increase of the mean impedance with increasing frequency was observed. Student's t-tests showed significant differences between 25 MHz and the higher frequencies. The same trend was found for the individual samples. However, the differences were only significant for the senium samples between 25 and 100 MHz. Significant differences between the samples were observed at 50 and 100 MHz. At 50 MHz the mean impedance of the female senium donor was lower compared to impedances of both male donors. At 100 MHz the difference was only significant between the senium samples.

Similar anisotropic impedance distributions were observed for all samples and all frequencies. In order to explore the complex relations between loading angle, impedance distribution and frequency, the normalized angular dependent histograms are represented as color coded contour plots for each frequency in Fig. 1. At 100 MHz the histograms for all angles have a symmetric shape. Width and peak values however varied considerably. Between 15° and 45° the distributions are broadened and the peak reaches a local maximum. In addition to the more irregular pattern an impedance downshift is apparent

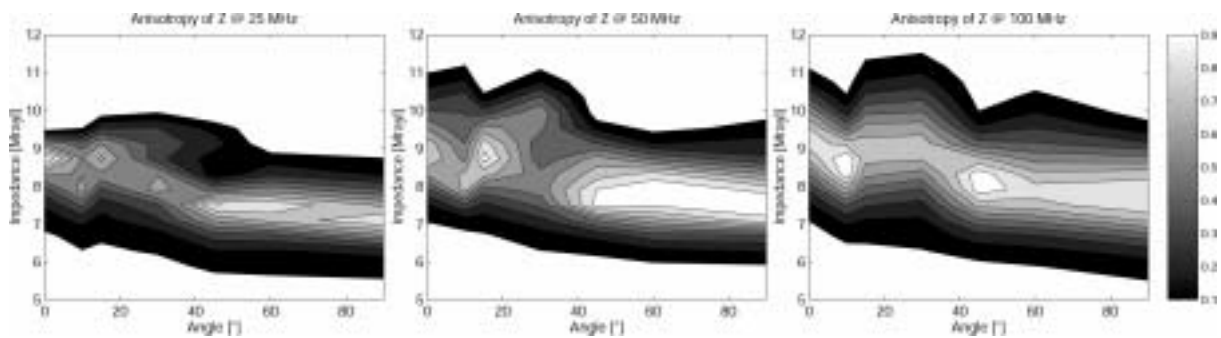


Fig. 1. Contour plots of the impedance histograms as a function of the loading angle.

particularly at 25 MHz. An anisotropy ratio AR was defined as the ratio between the maximum peak value to the peak value at 90° . The highest anisotropy was observed at 50 MHz ($AR = 1.32$; 1.23 for 25 MHz and 1.15 for 100 MHz 1.15).

Conclusions

The resolution of the 25 MHz transducer is not sufficient to separate the Haversian channels from the bone matrix. This in turn results in an underestimation of the acoustic impedance, which is dependent on number, size, distribution and content of these channels. However, since the lowest impedance values were observed for all samples with quite different morphological characteristics, it is hypothesized, that the lower values are also caused by dispersion. No significant differences were found between 50 and 100 MHz. Anisotropy was observed for all frequencies. Insufficient resolution again limits the reliability of the observations at low frequencies. The current results suggest, that artifacts resulting from the presence of cavities in cortical bone cannot be neglected. However, at 100 MHz and a lateral resolution of $20 \mu\text{m}$ these artifacts appear to be minimized. Nevertheless further quantitative analysis of morphological parameters is required in order to support this hypothesis.

Acknowledgments

This work is supported by the Deutsche Forschungsgemeinschaft under Grant BR 1348/4-3.

References

- [1] Bouxsein et al., Quantitative ultrasound of the calcaneus reflects the mechanical properties of calcaneal trabecular bone, *J. Bone Miner. Res.* **12** (1997), 839–846.
- [2] Chaffai et al., Ultrasonic characterization of human cancellous bone using transmission and backscatter measurements: relationships to density and microstructure, *Bone* **30** (2002), 229–237.
- [3] Chappard et al., Assessment of the relationship between broadband ultrasound attenuation and bone mineral density at the calcaneus using BUA imaging and DXA, *Osteoporos. Int.* **7** (1997), 316–322.
- [4] Han and Rho, Dependence of broadband ultrasound attenuation on the elastic anisotropy of trabecular bone, *Proc. Inst. Mech. Eng.* **212** (1998), 223–227.
- [5] Hans et al., Ultrasound velocity of trabecular cubes reflects mainly bone density and elasticity, *Calcif. Tissue Int.* **64** (1999), 18–23.
- [6] Laugier et al., *In vitro* assessment of the relationship between acoustic properties and bone mass density of the calcaneus by comparison of ultrasound parametric imaging and quantitative computed tomography, *Bone* **20** (1997), 157–165.

- [7] Lees and Klopholz, Sonic velocity and attenuation in wet compact cow femur for the frequency range 5 to 100 MHz, *Ultrasound Med. Biol.* **18** (1992), 303–308.
- [8] Raum et al., Quantitative SAM zur Bestimmung der akustischen Impedanz von kortikalem Knochengewebe, *Z. Med. Phys.* **9** (1999), 246–253.
- [9] Raum et al., Quantitative scanning acoustic microscopy of cortical bone using a multi layer analysis method, in *Proc. IEEE Ultrason. Symp.*, 1999, pp. 593–596.
- [10] Raum et al., Multi Layer Analysis – Quantitative scanning acoustic microscopy for tissue characterization at a microscopic scale, *IEEE Trans. on UFFC* **50** (2003), 507–516.
- [11] Smitmans et al., Variations in the microstructural acousto-mechanical properties of cortical bone revealed by a quantitative acoustic microscopy study, in *Proc. IEEE Ultrason. Symp.*, 2001, pp. 1379–1382.

Ultrasound Characterisation of Soft and Hard Biological Tissues

Ultrasound computer tomography for breast cancer diagnosis

Rainer Stotzka, Tim O. Müller, Klaus Schlote-Holubek and Hartmut Gemmeke
Forschungszentrum Karlsruhe, Institute for Data Processing and Electronics, Germany
Tel.: +49 7247 82 4738; E-mail: rainer@stotzka.de

Purpose: Ultrasound is the most available and most frequently used diagnostic imaging modality. In breast cancer diagnosis, ultrasound examination provides useful additional diagnostic information. Moreover ultrasound does not harm biological tissue and can be applied frequently. But conventional ultrasound imaging methods lack both high spatial and temporal resolution. The contrast and the resolution depend highly on the frequency used, as well as on the distance between the transducer array and the region of interest within the breast. Usually, the scanner is operated manually and the tissue is deformed while getting as close as possible to the region of interest. Therefore, image content and quality depend strongly on the operator. Exact measurement of tissue structures, like tumor size, is not possible.

The intention of the development of ultrasound computer tomography is to increase the reliability of ultrasound imaging and to supply standardized images similar to other imaging modalities like computer tomography (CT) and magnetic resonance imaging (MRI).

At Forschungszentrum Karlsruhe, we are developing an ultrasound computer tomography system for breast imaging.

Methods and materials: Ultrasound computer tomography (USCT) is a new imaging method which allows the recording of reproducible images with higher resolution and tissue contrast [1,2]. In conventional ultrasound imaging a linear transducer array is operated manually and only the tissue reflections are recorded.

In USCT the transducers are arranged in a fixed geometry (Fig. 1) around the object to be examined. For breast examinations the breast is placed in a tank filled with water as coupling medium. The transducers are mounted in a cylindrical array at the tank walls.

One transducer is acting as transmitter and emits a short pulse, which is scattered by the structures inside the object. Every transducer is small, emitting a nearly undirected beam (spherical wave front). All other transducers measure the transmitted, reflected and scattered signals (A-scans) simultaneously. The received signals are amplified, digitized and stored. Then the next transducer will transmit an ultrasound pulse while all others receive the signals and so on. Figure 2 shows the ring architecture of a two-dimensional ultrasound computer tomography system and an A-scan of one receiving element.



Fig. 1. Fixed arrangement of transducers for 3D ultrasound computer tomography. The transducers are arranged in a cylindrical array around a tank containing the object and water as the coupling medium.

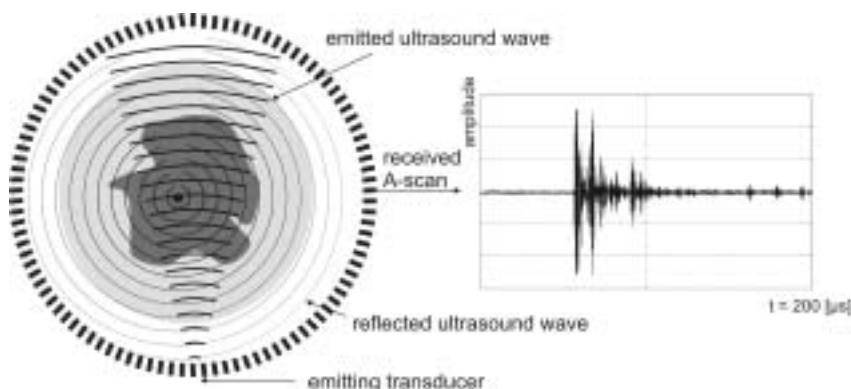


Fig. 2. Architecture of the USCT system built in our institute, shown in 2D. A ring (cylinder) of ultrasound transducers encloses the object (left). One transducer emits a short ultrasound pulse, all other transducers receive simultaneously. The A-scan at the right side shows the directly transmitted and scattered signals.

We have built an experimental setup to evaluate a multi-sensor system which regards transmitted, scattered and reflected waves at the same time. It consists of two transducer arrays (2.5 MHz) in a water tank, a pulse generator, an amplifier and a digital data acquisition system connected to an external computer. The signal processing and image reconstruction is done by the computer. Both transducer arrays can be positioned independently on the ring to emulate a full circular array (1600 elements, diameter 12 cm). An array consists of 16 elements each 0.2 mm wide, 10 mm high with a pitch of 0.25 mm. One array is used as the emitter, the other as the receiver. Every receiving element is treated separately. For every emitter position, all possible receiver positions on the circle are evaluated and the correspondent signals are recorded successively.

Based on the data recorded by our experimental setup we are able to reconstruct two-dimensional tomographic images. The reconstruction is based on a full aperture sum-and-delay algorithm [1] on the assumption of constant sound speed in the water and the object. Furthermore, no corrections of the angle-dependent sensitivity of the transducers have been applied.

Results: Since the measuring time for the simple prototype takes up to 10 hours, we needed fixed phantoms mimicking biological tissue. We created several phantoms from of a galantine and olive-oil emulsion with straws and threads as inner structures.

The whole imaging system is two-dimensional in a cylindrical slice with a height of about 1 cm and a diameter of 12 cm. For the phantom, we built a model sketched in Fig. 4 which we submerged inside

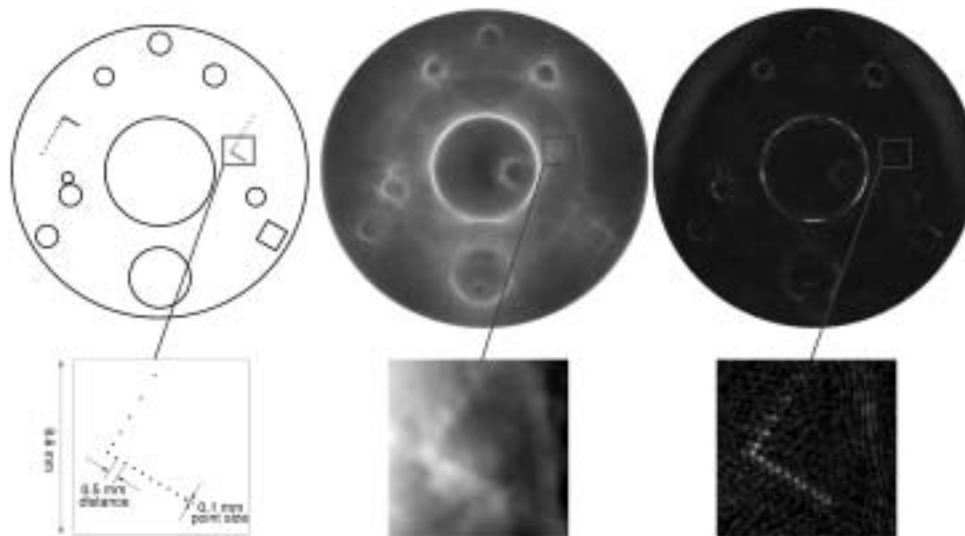


Fig. 3. Phantom and reconstructed images. Left: Rough plan of the phantom. The diameter is 8.5 cm. The smallest structures consist of nylon threads with a diameter of 0.1 mm and a spacing of 0.5 mm shown in the region enlargement below. Middle: Reconstruction using only amplitude information. Right: Reconstruction including phase information. The nylon threads are clearly visible.

a plastic cup with very thin walls. The smallest structures within the phantom are nylon threads with a diameter of 0.1 mm each, corresponding to approximately 0.2 wavelengths of the emitted ultrasound signal.

We have recorded the ultrasound signals of the phantom for 100 emitter positions and 1440 receiving positions each, gathering approximately 5 GBytes ultrasound data. Figure 3 shows the results of an image reconstruction. Two different types of images can be reconstructed: one using only the amplitude information of the scattered signals and the other including the phase information. Amplitude images show high contrast and low noise but their image resolution is limited to the length of the ultrasound pulse (approx. 1–1.5 mm). By inclusion of phase information the quality of imaging allows the visualization of structures as small as 0.1 mm, but the overall image is getting noisy.

Conclusions: Ultrasound computer tomography allows an operator independent and 3-dimensional imaging of tissue structures. The reconstructed images are of superior quality in comparison to common ultrasound imaging systems. More detailed structures are visible and there are no shadows hiding the view of remote tissue features. A measurement of geometric structures is possible with an accuracy of approximately 0.25 mm.

In future we will set up cylindrical geometry consisting of 1920 transducer elements [4] and a parallel data recording system to image biological tissue *in vivo*. Applied to breast tissue, ultrasound computer tomography promises high quality three-dimensional images without ultrasound shadowing artifacts. For the first time the premises for multimodal registration of 3D ultrasound images to other imaging modalities are fulfilled. It is now possible to register US images of the breast to MRI, CT and positron emission tomography or even X-ray mammograms using our algorithm proposed in [3].

References

- [1] R. Stotzka, J. Würfel and T. Müller, Medical imaging by ultrasound computer tomography, in *SPIE's Internl. Symposium Medical Imaging 2002*, 2002, pp. 110–119.

- [2] M. Ashfaq and H. Ermert, Ultrasound spiral CT for the female breast: First phantom imaging results, in 35. Jahrestagung der Deutschen Gesellschaft für Biomedizinische Technik, 2001.
- [3] T. Müller, N.V. Ruiter, R. Stotzka, H. Gemmeke, J. Reichenbach and W. Kaiser, Model based fusion of X-ray mammograms and MR-volumes of the female breast, Third Congress on MR mammography 2003, 2003.
- [4] R. Stotzka, G. Göbel and K. Schlote-Holubek, Development of transducer arrays for ultrasound-computertomography, SPIE's Intern. Symposium Medical Imaging 2003, 2003.

Ultrasound in Bone Biomechanics

Ultrasound and vibration to measure bone mechanical properties: An overview

G. Van der Perre and S.V.N. Jaecques

K.U. Leuven, Division of Biomechanics and Engineering Design, Celestijnenlaan 200A, B-3001 Leuven, Belgium

Tel.: +32 16 327096; Fax: +32 16 327994; E-mail: Georges.VanderPerre@mech.kuleuven.ac.be

Introduction: The clinical fields where bone mechanical properties need to be measured are briefly discussed. Well-known applications are osteoporosis detection, follow-up of fracture healing and distraction osteogenesis. Other applications can be found in tissue engineering and in the quantification of the fixation of dental and orthopaedic implants.

Vibration analysis basically measures resonance frequencies to determine the whole body stiffness (EI) of bone. If a long bone is considered as a slender beam, the resonance frequencies can be estimated from

$$f_n = \alpha_n \sqrt{\frac{EI}{ml^3}} \quad (1)$$

where f_n is the resonance frequency of a vibration mode n , α_n is a proportionality constant, EI is the whole body stiffness (more precisely the flexural rigidity), m is the mass and l the length [1]. The practical frequency range for bone is 0–1000 Hz.

Ultrasound velocity measurements (practical range 0.2–1 MHz for bone) allow the determination of material stiffness (E). In its most simplified form the basic equation is

$$c = \sqrt{\frac{E}{\rho}} \quad (2)$$

where c is the velocity of sound in the considered material, and ρ is the mass density.

Monitoring of callus consolidation: Vibration analysis can be used for monitoring of fracture healing; the tibia is presented as an example. The protocol involves weekly measurements of the resonance frequency of the first single bending mode (f_{SB1}) of both the fractured leg and the intact control leg. In a typical case, f_{SB1} is in the range 280–300 Hz for the intact leg. From five to seventeen weeks after fracture, f_{SB1} of the healing leg increased from 210 to 270 Hz. When the protocol is strictly followed, f_{SB1} shows a close relationship with the state of fracture healing and the evolution of f_{SB1} has proven to be more reliable and accurate than conventional clinical evaluation [2].

Table 1
Correlation between variables measured *ex vivo*

Correlation	Coefficient R^2
Femoral Strength (fracture load) – Trochanteric DEXA-BMD	0.88
Femoral Strength (fracture load) – Calcaneal US velocity	0.46
Femoral Strength (fracture load) – Calcaneal US attenuation (nBUA)	0.44
Vertebral Strength (fracture load LS3) – Vertebral DEXA-BMD	0.65
Vertebral Strength (fracture load LS3) – Calcaneal US velocity	0.21
Vertebral Strength (fracture load LS3) – Calcaneal US attenuation (nBUA)	0.18

Ultrasound velocity and attenuation measurements can be used for follow-up of bone quality during distraction osteogenesis. In clinical experiments, good agreement is found between the results of the ultrasound measurements and clinical conclusions drawn from radiographs.

Osteoporosis detection: US can be used as a non-invasive technique for in vivo detection of osteoporosis. In a large cadaver study on 70 individuals, correlations were examined between strength of bones and properties measured by US and dual energy X-ray absorptiometry (DEXA) [3]. Strength was measured in standardized mechanical test set-ups on iliac crest samples, whole lumbar spines, whole proximal femora and proximal femur samples. Quantitative US (QUS) was performed on the calcaneus because this is the bone examined in clinical US monitoring devices (e.g. Achilles[®] (Lunar), CUBA[®] (Norland/McCue), Sahara[®] (Hologic)). On all the abovementioned bones and bone samples, DEXA was used to measure bone mineral density (BMD).

For US, *ex vivo* correlations between calcaneal US velocity and femoral/vertebral strength were significantly lower than for DEXA [4], as illustrated in Table 1. However, calcaneal US seems to be a useful clinical tool to predict femoral/vertebral fracture risk [5,6]. This can be considered an “ultrasound paradox”.

Conclusions: Ultrasound and vibration (in comparison with imaging and absorptiometry) have the advantages of requiring low-cost and portable equipment, and are non-invasive measurements, not involving ionising radiation. Ultrasound and vibration are mechanical tests, and therefore provide direct mechanical information, as opposed to DEXA and other imaging techniques. Further research is needed but US and vibration are promising techniques regarding clinical applicability.

In recent research, vibration and ultrasound are used to stimulate bone remodelling and fracture healing. The application range is extended from purely diagnostic to therapeutic.

References

- [1] G. Van der Perre, Dynamic analysis of human bones, in: *Functional behaviour of orthopaedic materials*, P. Ducheyne and G.W. Hastings, eds, CRC Press, Boca Raton, FL, 1984, pp. 99–159.
- [2] Y. Nakatsuchi, A. Tsuchikane and A. Nomura, Assessment of fracture healing in the tibia using the impulse response method, *J. Orthop. Trauma* **10** (1996), 50–62.
- [3] X.G. Cheng, G. Lowet, S. Boonen, P.J. Nicholson, G. Van Der Perre and J. Dequeker, Prediction of vertebral and femoral strength *in vitro* by bone mineral density measured at different skeletal sites, *J. Bone Miner. Res.* **13** (1998), 1439–1443.
- [4] X.G. Cheng, P.H. Nicholson, S. Boonen, G. Lowet, P. Brys, J. Aerssens, G. Van Der Perre and J. Dequeker, Prediction of vertebral strength *in vitro* by spinal bone densitometry and calcaneal ultrasound, *J. Bone Miner. Res.* **12** (1997), 1721–1728.
- [5] D.C. Bauer et al, Broadband ultrasound attenuation predicts fracture strongly and independently of densitometry in older women. A prospective study. Study of Osteoporotic Fractures Research Group, *Arch. Intern. Med.* **157** (1997), 629–634.
- [6] D. Hans et al, Ultrasonographic heel measurements to predict hip fracture in elderly women: the EPIDOS study, *Lancet* **348** (1996), 511–514.

2. Biomechanics

High frequency and low amplitude mechanical loading as a countermeasure for bone loss in astronauts

K. Dierckx^{a,*}, J. Vander Sloten^a, P. Spaepen^a, B. Noble^b, G. Carmeliet^c and D.B. Jones^d

^a*Division of Biomechanics and Engineering Design, K.U.Leuven, Belgium*

^b*University of Edinburgh, Scotland, UK*

^c*Division of Experimental Medicine and Endocrinology, K.U.Leuven, Belgium*

^d*Department of Experimental Orthopaedics and Biomechanics, Philipps University, Marburg, Germany*

Introduction: Bone loss in astronauts during space flight is one of the major problems of manned space missions. One promising treatment consists of the mechanical loading of bones with vibrations of low amplitude and high frequency [6]. These vibrations seem to have an anabolic effect on trabecular bone even when they are applied only during a limited period of time per day. Tests on rats and sheep under gravitational conditions show extremely good results [5,6].

Methods: An experiment has been designed to test the hypothesis of the effect of high frequency and low amplitude stimulation based on an ex vivo trabecular bone tissue culture model [2] under microgravity. The experimental setup consists of six loaded bone samples and six controls and will be sent up in orbit with an unmanned Foton flight for approximately 14 days in spring 2006. The six bone samples will be loaded four times per day for 10 minutes with a periodic signal of 30 Hz and 50 μ strain.

MicroCT images will be taken before and after the flight and can be analysed by our computer models to investigate a possible effect of the applied mechanical loading. Structural parameters such as bone volume density, bone surface density and trabecular thickness will be compared before and after the loading of the bones [1]. If a difference can be seen between the bone structural parameters, these differences will be linked to our FEM models to simulate the resorption and formation of bone due to the mechanical loading [7].

All bone samples will be double labelled with calcein and tetracyclin in order to study histologically the new bone formation. These results can be matched to the results coming from the CT images [3]. Finally, also apoptosis of osteocytes will be studied since it has been stated that apoptosis is associated with local bone resorption [4].

Results: A special bioreactor, based on an existing bioreactor [2], has been developed (see Fig. 1). This bioreactor permits the mechanical load to be applied by the upper piston via a piezoactuator. Maximal displacement of the piezoactuator will be measured. Below the lower piston a force sensor will measure the mean dynamic force level. In this way, no bias is introduced by the friction between the piston and the bioreactor since this friction will be deviated to the frame of the loading system (Loading system not shown in Fig. 1).

Since the reactor is axisymmetric, it is also possible to make high quality microCT images of the bone samples without removing the samples from their sterile environment. Because of the axisymmetry, the inlet and outlet of the culture medium is below the bone sample. In order to make a good fluid flow

*Tel.: +32 16 32 70 62; Fax: +32 16 32 79 94; E-mail: Koen.Dierckx@mech.kuleuven.ac.be.

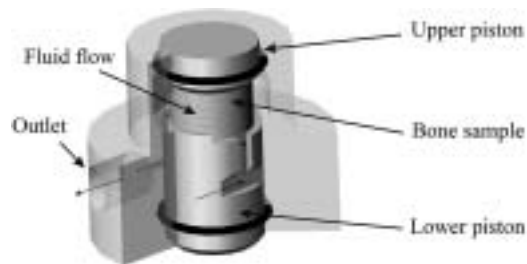


Fig. 1. New multifunctional bioreactor.

possible around the bone, the lower piston has been given a special shape. The medium (DMEM high glucose: internal communication from D.B. Jones) flows in via the lower piston and leaves the reactor on the other side so the medium will flow around the bone sample. Some additional dye tests have to be done to determine if this configuration is optimal to have a good diffusion of nutrients into the bone sample.

Work in the near future: In the near future, viability of the bone samples will be tested with an MTT assay after taking the samples to validate the sampling method (sawing, milling and drilling) and after taking microCT-images in order to determine the maximal possible resolution and radiation dose without having too much cell death.

The next step will consist of determining the optimal concentrations for the fluorescent labeling procedure together with the determination of the optimal parameters (displacement, frequency and force level) for mechanical loading.

Conclusion: A new bioreactor has been developed to study the effect of microgravity on trabecular bone. We will test the hypothesis that high frequency low amplitude mechanical stimulation of bone can be used as a countermeasure for bone loss in astronauts.

Possible spin-off applications of this high frequency stimulation of bones are the treatment of osteoporosis and tissue engineering with bone scaffolds. These high frequency vibrations could slow down the breakdown of bone in osteoporosis patients or could speed up the integration between the living bone and the scaffolds. A high throughput system for investigating different types of drugs is another possible application.

References

- [1] L.A. Feldkamp, S.A. Goldstein, A.M. Parfitt, G. Jesion and M. Kleerekoper, The direct examination of three-dimensional bone architecture *in vitro* by computed tomography, *Journal of Bone and Mineral Research* **4** (1989), 3–11.
- [2] D.B. Jones, E. Broeckmann, T. Pohl and E.L. Smith, Development of a mechanical testing and loading system for trabecular bone studies for long term culture, *European Cells and Materials* **5** (2003), 48–60.
- [3] R. Muller, H. Van Campenhout, B. Van Damme, G. Van Der Perre, J. Dequeker, T. Hildebrand and P. Rueggsegger, Morphometric analysis of human bone biopsies: a quantitative structural comparison of histological sections and micro-computed tomography, *Bone* **23**(1) (1998), 59–66.
- [4] B.S. Noble, N. Peet, H.Y. Stevens, A. Brabbs, J.R. Mosley, G.C. Reilly, J. Reeve, T.M. Skerry and L.E. Lanyon, Mechanical loading: Biphasic osteocyte survival and the targeting of osteoclasts for bone destruction in rat cortical bone, *Am J Physiol Cell Physiol* **10** (2002), 1152.
- [5] B.S. Oxlund, G. Ortoft, T.T. Andreassen and H. Oxlund, Low intensity, high-frequency vibration appears to prevent the decrease in strength of the femur and tibia associated with ovariectomy of adult rats, *Bone* **32** (2003), 69–77.
- [6] C. Rubin, S. Turner, S. Bain, C. Mallinckrodt and K. McLeod, Extremely low level mechanical signals are anabolic to trabecular bone, *Nature* **412** (2001), 603–604.

- [7] H. Van Oosterwyck, J. Vander Sloten, R. Puers and I. Naert, Finite element studies on the role of mechanical loading in bone response around oral implants, *Meccanica* **37** (2002), 441–451.

Investigations of the solidification of glass ionomer cements containing calcium fluoroalumosilicate glasses

N. Friede*, J. Trempler and H. Roggendorf

Institut für Werkstoffwissenschaft, Martin-Luther-Universität Halle-Wittenberg, Halle, Germany

Tel.: +49 3461 46 3739; Fax: +49 3461 46 3839; E-mail: hans.roggendorf@iw.uni-halle.de

Introduction: Glass ionomer cements are applied for dental restorations [1,4] for more than 20 years. They consist of a powdered glass – usually calcium fluoroalumosilicate glasses with low alkali contents – that reacts with polyelectrolytes to a solid polymeric matrix. The hardening reaction consists of two important steps. The first is the partial dissolution of the glass. The second is the precipitation of a polymer matrix by the interaction between the ions dissolved from the glass and a polymer acid like polyacrylic acid or itaconic acid. The cations bond the anionic groups of the polymer chains by electrostatic forces. The result of the process is a composite material consisting of a polymeric matrix with embedded glass particles. The kinetics of the hardening reactions of the glass ionomer cements are important for their application: The kinetics should be slow enough to allow handling of the cements in a dentists session, but should be fast enough to yield an appreciable strength within a short time. Additives like tartaric acid are used to regulate the setting behaviour of the cements.

Methods: The chemical composition of the glasses was reduced to the three-component $\text{CaF}_2 - \text{Al}_2\text{O}_3 - \text{SiO}_2$ system which contains the essential components of commercial glasses used in glass ionomer cements. 22 glasses of this system with systematically varied composition were molten at 1500°C , cooled fairly rapidly by pouring on a hot (350°C) metal plate, characterised and milled to glass powders. The composition ranges were: 25 to 50 wt % SiO_2 , 22 to 48 wt % CaF_2 , and 20 to 40 wt % Al_2O_3 . Crystallisation during cooling was investigated to determine the phase composition of the glasses and to calculate the chemical composition of the glass matrix. The dissolution behaviour of the glasses was tested in acidic corrosion media like 0.5 M HCl and 0.5 M polyacrylic acid. 0.5 g of the glass powder (fraction $<63 \mu\text{m}$) was dispersed in the leachant by stirring for 0.25 or 2 h at 20°C . The compressive strength of glass ionomer cements, which were made from mixtures of glass powders of all 22 glasses with tartaric acid and polyacrylic acid as further components, was tested according to DIN EN 29917. Commercial products were tested for comparison.

Results: The crystallisation and dissolution behaviours of the glasses depend on the glass composition. CaF_2 (fluorite) crystallised in glasses with fluorine contents > 35 wt % [2] during the applied cooling routine. Glasses with technically relevant compositions dissolved congruently in acidic media, which means that the concentration relations of the glass components in glass matrix and leachate are similar. The congruent dissolution in acids – which is not the usual behaviour of ordinary silicate glasses [3] – can be explained by the low degree of inorganic polymerisation of the respective glass structures. The kinetics of the corrosion process are correlated to the composition of the glass matrix. The highest corrosion rates were found for glasses with high CaF_2 contents of the glass matrix. Figure 1 shows the

*Present address: Wacker-Chemie, Burghausen, Germany.

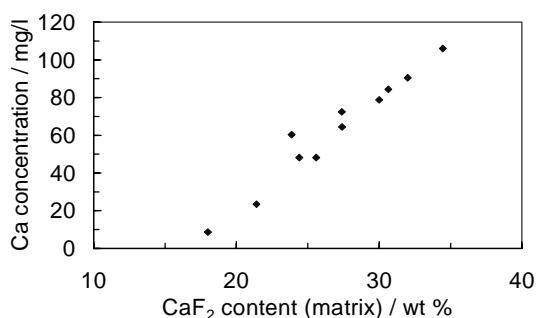


Fig. 1. Ca concentration in the leachate of corroded glass powders; corrosion: 0.5 g glass powder dispersed in 50 ml 0.5 M polyacrylic acid at 20°C; corrosion time: 2 h.

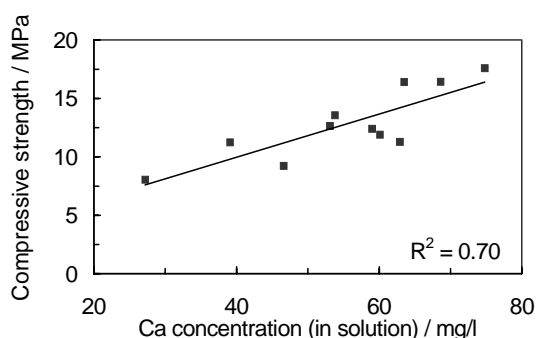


Fig. 2. Correlation between compressive strength of glass ionomer cements (after hardening) with Ca^{2+} release rates in laboratory corrosion tests.

accumulated Ca content in the leachate as a function of the glass matrix composition. Crystallisation of CaF_2 lowers the concentration of the respective component in the glass matrix and thus reduces the corrosion kinetics. Al^{3+} precipitates during corrosion in polyacrylic acid, which indicates its importance for the matrix formation.

The compressive strengths of commercially available glass-ionomer cements yielded values from 70 to 180 MPa dependent on the kind of material, whereas the laboratory materials obtained values up to 30 Mpa. The reason for this discrepancy is that the other components of the laboratory cements were not optimised with respect to the specific glass composition. The correlation between mechanical properties and the data of the glass corrosion tests stressed the importance of cations like Ca^{2+} and Al^{3+} for the solidification of the glass ionomer cements. Figure 2 shows the correlation between the strength of the glass ionomer cements and the release rates of Ca^{2+} in polyacrylic acid measured in laboratory tests.

Similar results were obtained for Al^{3+} , whereas the results concerning Si^{4+} were ambivalent. This is possibly due to the stabilising effect of SiO_2 on the glass structure. High SiO_2 contents led to low cation releases and thus to low strengths. On the other hand, a positive correlation between Si^{4+} release in polyacrylic acid and compressive strength of the cements was found. The results indicate that the stability of the polymer matrix increases with the charge density of the cations (cationic “field strength”).

Acknowledgements: The mechanical properties were tested in the laboratories of Prof. Dr. W. Grellmann, Martin-Luther-Universität Halle-Wittenberg.

References

- [1] M. Braden, *Polymeric dental materials*, Springer, Berlin, 1997.
- [2] N. Friede and H. Roggendorf, (Proc. 7. Int. Otto-Schott-Colloquium) *Glass Sci. Technol.* 75C2, 2002, pp. 109–114.
- [3] H. Scholze, D. Helmreich and I. Bakardjiev, *Glastech. Ber.* 48 (1975), 237–247.
- [4] A.D. Wilson and J.W. McLean, *Glasionomerzement*, Quintessenz Verlags-GmbH, Berlin, 1988.

ESB Satellite Symposium: Biofluidmechanics

Hemodynamic study in 26 authentic carotid bifurcations

L. Goubergrits, K. Affeld, J. Fernandez-Britto and L. Falcon

Humboldt University, Berlin, Germany

Tel.: +49 30 450553808; Fax: +49 30 450553938; E-mail: leonid.goubergrits@charite.de

Introduction: The carotid bifurcation is of special interest because of its frequent atherosclerotic wall alterations and because of its complex flow properties. Observations have shown that wall alterations correlate with regions of low wall shear stress. Furthermore, investigations have shown significant variations in geometric parameters among individuals. These variations can contribute to a corresponding variability in the hemodynamics, which affect the atherosclerosis. However, the quantitative correlations between alterations, geometry and flow parameters are not yet known.

Methods: At the post mortem study 86 vessel casts of the carotid artery from 64 autopsies were fabricated. The autopsies were performed at the Department of Pathology, Dr. Finlay Hospital, Havana, Cuba. For each autopsy case the etiologic data about sex, age and disease were collected. The collected data of all autopsy subjects were presented earlier [1,3]. The apparatus and the procedure of the vessel casts fabrication were presented elsewhere in detail [2]. After the fabrication of the vessel casts a pathomorphological analysis of the vessel wall was performed and atherosclerotic wall alterations in regard to distribution and level were assessed. The qualitative analysis of each lesion type – fatty streak, fibrous plaque and severe (complicated and calcified) plaque – was made. A quantitative analysis of the assessed wall alteration was performed using atherometric system. A more detailed description of the atherometric system variables was published in [2]. The vessel casts are an exact replicas of the vessel lumen and can be used to measure geometric parameters and geometry digitalization for further numerical study. Altogether 26 vessel casts from 20 autopsy subjects were digitized with an optical method on the basis of the structured light lines and three-dimensional computer models were generated. These models were imported by the computational fluid dynamics (CFD) program FLUENT in order to reconstruct the blood flow of the individual vessel geometry. The geometric parameters known as possible risk factors were assessed from vessel casts and computer models. These are the diameter of the carotis communis D_c , the diameter of the carotis externa D_e , the diameters of the carotis interna at proximal D_{i1} and distal parts D_{i2} , the curvatures in each carotid branch, the external branch angle between carotis communis and carotis interna, the internal branch angle between carotis communis and carotis interna and non-planarity angle. Two further parameters were introduced: the carotid sinus enlargement $En_1 = D_{i1}/D_c$, and the total bifurcation enlargement $En_2 = (D_{i1}^2 + D_e^2)/D_c^2$.

In order to reconstruct the flow, the digitized data of the vessel casts were imported by a pre-processor Gambit™ (Fluent Inc., USA), which was used to create automatically an unstructured surface mesh of

triangles. The surface mesh was then imported into another pre-processor TGrid (Fluent Inc., USA), which was used for improvement of the surface mesh and automatic generation of an unstructured computational mesh of about 400,000 tetrahedral cells. This fine mesh allows also a very good resolution of the recirculation regions. The computations of the stationary blood flow in reconstructed vessels with rigid walls were performed with the flow solver FLUENT6. The study under pulsatile conditions is possible, but requires a large computational and post-processing efforts for a large number of investigated objects (26 in our study). Furthermore the simulations under pulsatile conditions by other researchers, revealed no significant differences between pulsatile and non-pulsatile simulation for investigated parameters: locations and areas of low wall shear stress. The simulation is based on the three-dimensional Navier-Stokes equations for incompressible Newtonian fluid flow. All simulations were done with a second order upwind discretization scheme for the convective terms of the Navier-Stokes equations. Pressure-velocity correction method SIMPLEC was used. The kinematic viscosity of the fluid model was set to $\mu = 3.5 \times 10^{-6} \text{ m}^2/\text{s}$. No-slip boundary condition was set at the walls. For each artery the simulations under diastolic and systolic conditions were performed. The Reynolds number was set to $Re = 200$ for diastole and $Re = 700$ for systole. The inflow was defined as a parabolic velocity profile. The outflows were defined as a constant pressures, different for each branch, thus defining the flow ratio of the internal and external branches at 55:45 for systole and 75:25 for diastole. The results of the numerical simulation are the flow parameters such as velocity, pressure and wall shear stress as a function of space only.

Results: Correlation analysis between geometric parameters and areas with low wall shear stress using linear regression technique was performed under consideration of etiologic and morphometric data. The correlation analysis of the geometric, etiologic and morphometric data are published earlier [4]. The analysis showed that no correlations were found between areas with low wall shear stress and any measured angle (internal and external branch angles, total bifurcation angle and non-planarity angle). The square of the Pearson's correlation coefficient R^2 was lower than 0.001. No correlation was found for normalized distal diameter of the carotis interna D_{i2}/D_c ($R^2 = 0.023$). Some tendencies were found for normalized proximal diameter of the carotis interna or carotid sinus enlargement $En_1 = D_{i1}/D_c$, curvatures and normalized diameter of the carotis externa D_e/D_c . The correlation coefficients of all these parameters were about $R^2 = 0.25$. Relative high correlation coefficient with $R^2 = 0.46$ was found only for one geometric parameter. This is the total bifurcation enlargement En_2 . Further considerations found that the parameter $M = (En_2 - 1)^2$ is the main geometric risk factor. This is a so called loss parameter for sudden duct expansion.

Conclusions: With the application of proposed methods, the atherosclerotic wall alterations, geometry parameters and wall shear stress distributions can be assessed and analyzed in order to find the qualitative correlations between them. If one considers to that a small variation in the geometry shape can influence and change the flow pattern, then one must agree that investigations with averaged or simplified geometry cannot be sufficient. This can only mean investigating an individual vessel.

The next step of this study are the flow simulations under the pulsatile conditions. The unsteady simulations allow the assessment of the other hemodynamic parameter, which may be considered as possible risk factor. This parameter is the oscillating shear stress.

References

- [1] L. Goubergrits, K. Affeld, J. Fernandez-Britto and L. Falkon, Atherosclerosis in the Human Common Carotid Artery. A Morphometric Study of 31 Specimens, *Pathol Res Pract* **197** (2001), 803–809.

- [2] L. Goubergrits, K. Affeld, J. Fernandez-Britto and L. Falkon, Geometry of the Human Common Carotid Artery. A Vessel Cast Study of 86 Specimens, *Pathol Res Pract* **198** (2002), 543–551.
- [3] L. Goubergrits, K. Affeld, J. Fernandez-Britto and L. Falkon, Atherosclerosis and flow in carotid arteries with authentic geometries, *Biorheology* **39**(3,4) (2002), 519–524.
- [4] L. Goubergrits, K. Affeld, J. Fernandez-Britto and L. Falkon, Investigation of geometry and athero-sclerosis in the human carotid bifurcation's, *J. of Mech. in Med. and Biology* **3**(1) (2003), 31–48.

Biofluid Mechanics

Non-linearities of the pressure-volume-relation of the perilymphatic space of the guinea-pig

E.J. Haberland^{a,*} and H.J. Neumann^b

^aDepartment of Ear, Nose, Throat, Head and Neck Surgery, University of Halle, Germany

^aDepartment of ENT and HNS, City Hospital "Martha-Maria", Halle (Saale), Germany

Introduction: Slow and fast volume displacements of the perilymphatic fluid are caused by sound and vibration via the eardrum and via physiological coupling, e.g. of the heart action, respiration, muscle reflexes and changes of body position. Following this influences perilymphatic pressure will change as well. In experiments we observed, that the pressure-volume-function is dependent of the value of static pressure. The passive pressure characteristics of the perilymphatic system takes into account non-linearities and valve characteristics in the convection-relevant slow and ultra-slow movements of perilymph.

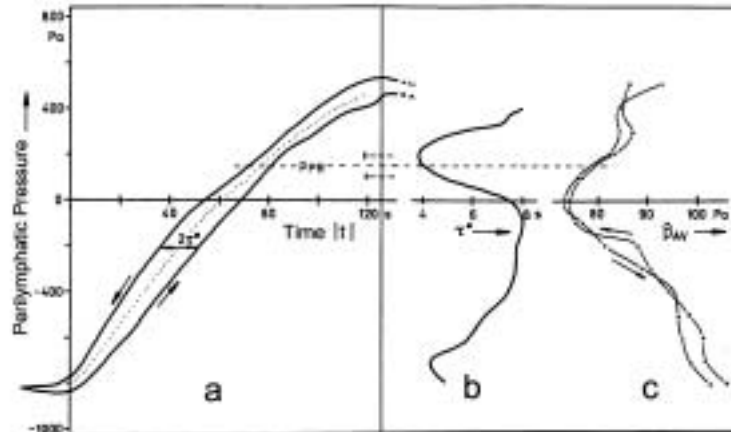


Fig. 1. (a) Pressure response of the perilymph system with about linear alteration (dashed line) of the inflow and outflow of artificial perilymph, (b) pressure dependence of the graphically determined time-constants τ^* from (a) and, (c) incremental pressure-impulse response p_{AV} to 42 nl volume-pulses into the cochlea as an evaluation of the reciprocal compliance.

*Address for correspondence: Ernst-J. Haberland, PhD, Department of Otorhinolaryngology, Head and Neck Surgery, Martin-Luther-University Halle-Wittenberg, Magdeburger Str. 12, D-06097 Halle, Germany. Tel.: +49 345 5571642; Fax: +49 345 557 1859; E-mail: ernst.haberland@medizin.uni-halle.de.

Methods: To show this pressure dependence we measured pressure responses to slow (about 1 min) and ultra-slow changes of perilymphatic infusion and superposed incremental fast volume pulses (400 ms and shorter, but below the audible range) into the same system. Experiments were carried out on spontaneous breathing guinea pigs in a Ketamine anaesthesia combined with local anaesthetics. Physiological functions, for example the reflex activity, remain unchanged.

Results: In small ranges of positive and negative static pressures are breaks in the pressure-volume characteristic (Fig. 1). Explanations for these properties are (i) the existence of a direction dependent variable flow through the aquaeductus cochleae, perivascular, perineural and other gaps, (ii) non-linear elastic properties of the membranes of the inner ear and capillary walls and (iii) variable viscosity of the moving fluids.

Conclusion: These investigations complete earlier calculations with a common model of the passive pressure response of the inner ear system [1] by consideration of break points of pressure-volume characteristics [2].

References

- [1] R. Franke and A. Dancer, Cochlear mechanisms at low frequencies in the guinea pig, *Arch Oto-Rhino-Laryngol* **234** (1982), 213–218.
- [2] H.J. Neumann and E.J. Haberland, Biophysikalische Untersuchungen der Perilymphbewegung und Sauerstoffdiffusion im cochleären Perilymphraum unter pathophysiologischen Bedingungen. Eine tierexperimentelle Studie. [Biophysical investigations of perilymph movement and oxygen diffusion in the cochlear perilymphatic space under pathophysiological conditions. An animal experimental study], Tectum Verlag, Marburg, 1998.

Investigations on skull deformation due to halo-frame placement

Th. Hierl^a, G. Wollny^b, F. Kruggel^b, I. Wojan^c, F. Dehn^c and W. Schmidt^d

^aDepartment of Oral & Maxillofacial Plastic Surgery; University of Leipzig, Leipzig, Germany

^bMax-Planck-Institute of Cognitive Neuroscience, Leipzig, Germany

^cInstitute for Structural Concrete and Building Materials, University of Leipzig/Materials Research and Testing Laboratory, Leipzig, Germany

^dInstitute of Anatomy, University of Leipzig, Germany

Tel.: +49 341 9721100; Fax: +49 341 9721109; E-mail: hiet@medizin.uni-leipzig.de

Introduction: Halo-frames are external devices fixed with screws to the skull which are used for medical purposes (e.g. traumatology, neurosurgery, or as in our department as a means to anchor a midfacial distractor [1]). Acting like a clamp fixed with a given torque on the skull, the question was to investigate on the impact of halo-frame placement on the skull. Furthermore, methods to visualize possible skull deformation and to simulate skull reactions in relation to forces and placement had to be developed.

Methods: In 12 patients the routinely obtained CT-scans (before treatment, at the end of treatment with fixed halo-frame) were used to visualize actual changes of the skull and for simulation purposes. To show and analyze real bony changes, a tool chain was developed which consists of preprocessing, non-rigid registration and visualization. A model based on fluid dynamics was used to ensure topology preservation of the objects in the study image. To visualize shape changes of the skull deformations

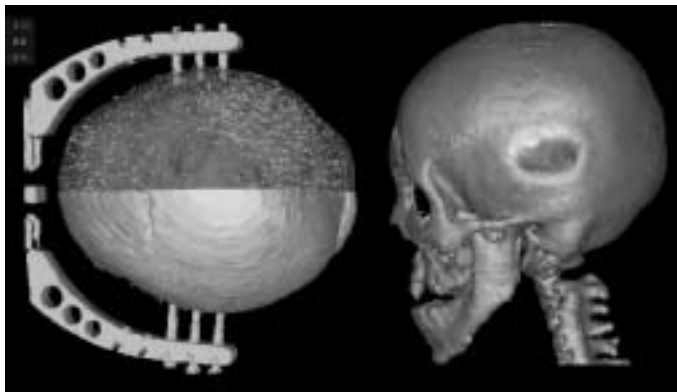


Fig. 1. On the left actual shape changes of a skull are visualized by way of skull displacement vectors and colour-coding. FEM-simulation of a skull deformation is shown on the right. Inward deformation is visualized as red, yellow and green, outward bulging as light blue.

of the derived triangle mesh were represented by the deformation vectors displayed as arrows on the surface model. Furthermore, a colour-coded display showed inward or outward shape changes [2]. For simulation of skull changes the preoperative CT-scans were utilized in a FE-model [3]. Here several problems have to be considered: Whereas the position of the halo-frame could be easily derived from the subsequently taken CT-scan, tests had to be made to calculate the real forces exerted on the skull. As the torque to fix the screws of the halo-frame was known (0.3–0.4 Nm) the correlation of force and torque was measured and showed to be linear. Material properties were taken from literature.

Results: The analysis of actual bony changes by way of the viscoelastic model showed a wide range from almost negligible changes up to 5 mm alterations. A typical example is given in Fig. 1. FEM-simulation lead to qualitative similar changes but failed with respect to quantitative data.

Conclusion: Halo-frame placement may lead to distinct changes in skull form. Here our novel tool chain allows an precise analysis. The failure of the finite-element-model with respect to quantitative changes may be due the application of uniform “material characteristics” in an heterogeneous patient sample (children-senior patients). Therefore the use of individualized material parameters might be a solution in future investigations.

References

- [1] T. Hierl, N. Klisch, R. Klöppel and A. Hemprich, Therapie ausgeprägter Mittelgesichtsrücklagen mit Hilfe der Distractionsosteogenese, *Mund Kiefer GesichtsChir* 7 (2003), 7–13.
- [2] G. Wollny, Th. Hierl, F. Kruggel and R. Klöppel, Die Analyse von Zeitreihenaufnahmen am Beispiel einer suturalen Mittelgesichtsdistraktion, in: *Bildverarbeitung für die Medizin 2002*, M. Meiler, D. Saupe, F. Kruggel, H. Handels and T. Lehmann, eds, Springer-Verlag Berlin, Heidelberg, 2002, pp. 63–66.
- [3] U. Hartmann, F. Kruggel, T. Hierl, G. Lonsdale and R. Klöppel, Skull mechanics simulations with the prototype SimBio environment, in: *Proceedings of the 1st. MIT Conference on Computational Fluid and Solid Mechanics*, (Vol. I), K.J. Bathe, ed., Elsevier Amsterdam, New York, Oxford, 2001, pp. 243–246.

M4 Tissue Engineering and Mechanobiology

Determination of the grip force distribution in functional grasping

A. Kargov, C. Pylatiuk, J. Martin and S. Schulz

Institute for Applied Computer Science, Germany

Tel.: +49 7247 82 6113; Fax: +49 7247 82 5786; E-mail: kargov@iai.fzk.de

Introduction: Information on the force exerted during grasping is essential for clinical evaluation of hand function, the biomechanical modelling of the hand and can equally be used for design optimisation of prosthetic hands [1]. Data on the distribution of grip forces are lacking. Therefore, sensors are needed, which are sufficiently durable, accurate, and compact to be attached to the palmar surface of the hand without significantly affecting manual dexterity.

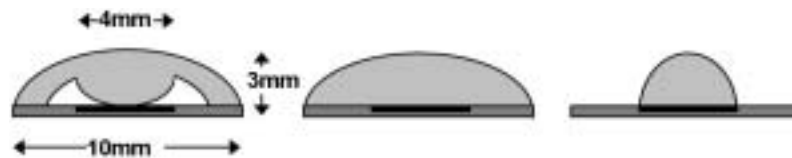


Fig. 1. Different designs of sensor domes.

Methods: A suitable force sensor includes a conductive polymer sensor [2] bonded on a thin rigid base plate in order to prevent bending of the sensor during measurements. The sensor is made of three plastic films coated with semiconductor layer and works as a pressure sensor. The resistance of this sensor changes under pressure applied. For the measurement of the grasp force the sensing area of a polymer sensor is modified with a silicone-rubber dome (Fig. 1) providing force-to-pressure transduction. Before the measurement the sensors were calibrated using precision digital scales for a range of 0–30 N and the force-resistance characteristic of the constructed sensor were obtained. Using this characteristic the applied grasp force is computed from the output signal of a voltage divider, which consists of the sensor with variable resistance and a fixed resistor (20 KOhm). By measuring the output voltage from a fixed resistor at low contact force up to 5 N the resolution of the sensor is higher. The grasp force is measured for the hands of 14 healthy subjects. Twenty sensor positions were predefined on the hand. They include all phalangeal pads of each finger, metacarpophalangeal joints and hypothenar surface of the palm. The definition of the measurement positions is the same for different sized hands, because all sensors were placed directly to the palmar surface of the hand independently from each other. Therewith the implementation of any measurement gloves, which cause the displacement of the force sensors and hinder the natural dexterity during grasping, was not required. Due to a minimised dimension of the sensor an adaptability of hand fingers during grasping was not disturbed. Six different grasping activities were selected, each one representing a functional prehension pattern. These are power grasp, extension grasp, tripod grasp, two-finger tip grasp, lateral grasp and spherical grasp, that are used in daily living [3]. The grasped object had to be held stable without excessive force for each prehension type. Each measurement was repeated 10 times.

Results: Two different solid dome types are compared to a construction with the shape of an inversed dome (Fig. 1). All the three dome types are suited for the measurement of contact forces, that applied vertically to the sensing area. Whereas at low forces applied at an angle of 45 degrees to the sensing area

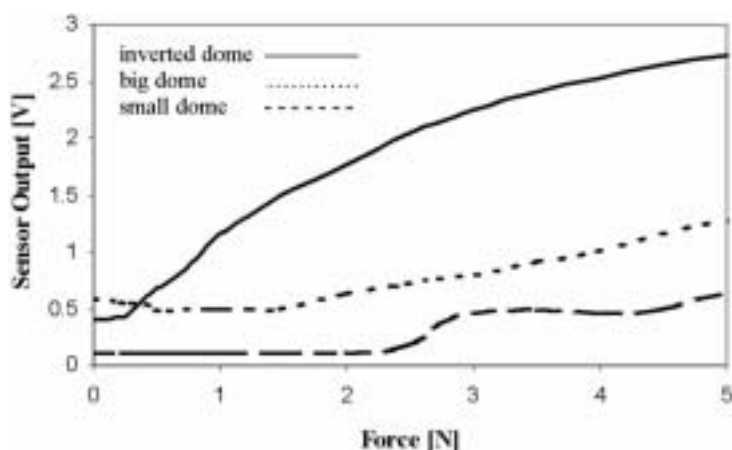


Fig. 2. Typical sensor output characteristics.

the solid dome types show a declination or no reaction at the output voltage characteristics (Fig. 2, broken lines). The inverse dome type (solid line in Fig. 2) shows a sufficient resolution even at low contact forces above 0.2 N, that applied vertically and angular to the sensing area. Therefore, this sensor type was chosen for the measurement of the grasp force distribution. The measurement data was obtained computer-aided. A statistical evaluation of the measured data is carried out and an arithmetic mean value and a standard deviation value are computed. There were not all predefined sensors in contact during grasping and the number of sensors in contact differs from subject to subject for each grasp. During grasping a bottle of water (power grasp) with a diameter of 88 mm and a weight of 1600, an average local contact force of 1 N for 19 out of 20 positions is measured. The contact force distribution varies on the palm. The value of contact force at the metacarpal region is lower than on the fingertips. The variability of the exerted forces in the same subject from measurement to measurement (an average standard deviations of 0.27) is smaller than inter-subject variability (an average standard deviation of 0.73). In all prehension tasks the average local contact force did not exceed 5.9 N. This maximum force is measured at the distal phalangeal pad of the index when opening and closing a zip with a two-finger tip grasp. Complex loading patterns are associated with typical prehension patterns of daily life.

References

- [1] A. Kargov, C. Pylatiuk, J. Martin and S. Schulz, A Comparison of the Grip Force Distribution in Natural Hands and in Prosthetic Hands. Proc. of the ISPRM 2003, Prague, 2003, pp. 241–244.
- [2] FSRTM, Tech. Rep., International Electronics & Engineering, Luxemburg, 2002.
- [3] C. Sollermann, Sollerman hand function test. A Standardised method and its use in tetraplegic patients, *Scand J Plast. Reconstr. Hand Surg.* **29** (1995), 167–176.

Manufacturing and coating of pastilles by a novel crystallization processes

J.-W. Kim and J. Ulrich

Martin-Luther-Universität Halle-Wittenberg, Fachbereich Ingenieurwissenschaften, Institut für Verfahrenstechnik/TVT, Halle (Saale), Germany

Tel.: +49 3461 46 3877; Fax: +49 3461 46 2788; E-mail: Joachim.ulrich@iw.uni-halle.de

Introduction: During the last several decades crystallization technologies have widely been applied in fields of purification and separation of substances. The field of applications of crystallization processes is, however, now a days growing. Interest is coming e.g. from areas such as the production of crystalline-formed medicines and the control of drug delivery systems [1,2].

Up to today pastillation processes are widely used to obtain the crystalline dosage (pastilles). However, no investigation was done to develop a deformation process of pharmaceutical materials under consideration of their crystallization times. The crystallization time is the most important parameter for the selection of the optimum production rate and the design of a solidification technology. The first part of this work, therefore, describes the role of the contact angle to control, the size and shape of pastilles and the crystallization time of drops to help to design the solidification technology. Another common method to control drug delivery system in pharmaceutical industry is an atomization coating process. The process is, however, still not optimal since there are problems such as cracking and splitting on the surface of the coating and there are non-uniformities in thickness of the coatings. In the second part of this work, therefore, a crystallization process is applied to produce crystalline-formed coatings. Crystalline coatings should solve the a.m. problems. It will be demonstrated that the surface nucleation of heterogeneous seed particles and the coating mechanism in the supersaturated solution are good alternating. Finally optimum operating conditions are determined by means of an investigation of the effect of operating.

Methods: A batch scale pastillation experiment is carried out. Pharmaceutical-grade bisacodyl ($C_{22}H_{19}NO_4$) is used as feed materials. The static contact angle between drop and substrate, the diameter of drop and the verticals height of drop are measured by the drop shape analysis system. A sequence of pictures describing the impact process is taken by a high-speed camera. A crystallization apparatus is used for the production of crystalline coatings. Isomaltulose ($C_{12}H_{22}O_{11}$) and distilled water are chosen as coating material and solvent, respectively. The solubility of Isomaltulose/water system and the nucleation behaviour is measured at various temperatures. The pastilles produced by the pastillation process are used as heterogeneous seeds (core materials). The interfacial tension as a function of the surface characteristic of the seed particles and the concentration of coating material is measured by the pendant drop method. A SEM technique is used to measure growth rates of the layer thickness of the crystals representing the coating. Furthermore, the surface morphology and the structure of core materials and coatings are studied, respectively.

Results: Figure 1 shows produced Bisacodyl pastilles that result from impacting of drops on a cooled substrate. The pastilles shown a narrow size distribution and a hemi-spherical form. It is found that the shape and size of pastilles strongly depends on chemical and physical properties of the material and the experimental conditions. The contact angles between a single drop and the surface are investigated at different experimental conditions which are: Reynolds number, degree of subcooling and characteristic of used surface. The static contact angle increases with increasing degree of surface roughness. It, however, decreases with increasing Reynolds number and degree of subcooling.

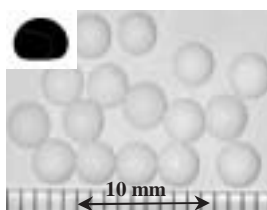


Fig. 1. Produced Bisacodyl pastilles.

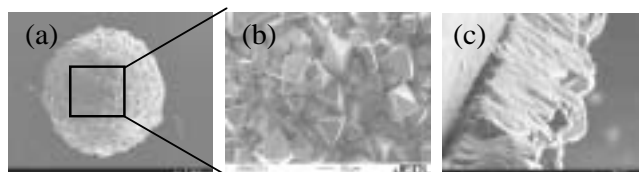


Fig. 2. Crystalline coating, surface morphology and surface cross section of coating.

The phenomenon of spreading and rebounding of drops is elucidated with regards to an energy balance of impacting drops and was the basis to discuss the deformation process. Using Madejski's model the degree of deformation is increased with increasing Reynolds number proportional to the 0.2 power. A simple drop solidification model allows to numerically study the degree of deformation based on the achieved experimental data. In case of pure Bisacodyl, it was found that normalized deformation and crystallization times are proportional to the Reynolds number to the power of 1.23. The normalized crystallization time is about 25 times higher than the normalized deformation time. On basis of the crystallization time the solidification equipment can be designed.

A new coating process was developed by solution crystallization. It was experimentally found how the crystalline coating can be formed and how the operating conditions effect the surface morphology and the crystal growth rate of the coating. The metastable zone width of the binary system of Isomaltulose/water is measured. It is experimentally found that a big width of metastable zone is essential for a good coating. It is, moreover, found that the phenomenon of coating of a seed particle is defined by a few steps: (1) the generation of a high number of nuclei on a surface of a seed particle (surface nucleation) (2) an agglomeration of nuclei on the surface of seed particles and (3) a growth combining the agglomerated nuclei together to form a layer on the surface of the heterogeneous seed. Figure 2 shows the productions of a crystalline coating, surface morphology and cross section of coating. Effective crystalline coatings and uniform surface morphologies (see Figs 2(a) and (b)) are achieved. The crystal layer (see Fig. 2(c)) is found very compact and without porosity and cracking in the structure of the coating. The crystal growth is influenced by the interfacial tension related to the surface characteristic of the used seed particles and the concentration of the coating material. The growth rate of the coating is increased with an increasing value of interfacial tension of the used seed particles. It is, however, only increased to a certain extent of concentration and than it begins to decrease because of a high number of nuclei. The growth rate of the coating on the surface of seed particles is increased with the increasing degree of subcooling, with increasing retention time and with decreasing agitation speed. The overall growth rate on the surface of the Bisacodyl particles in the Isomaltulose/water system is proportional to the supersaturation to the power of 5.7. The optimized conditions are found experimentally.

Conclusion: Melt and solution crystallization processes are applied to help to design a solidification technology and to develop a new coating technology. The size and shape of pastilles can be controlled

by the role of the contact angle. The deformation and crystallization times are numerically found. It has been proven that a crystallization coating technology can successfully be applied to produce crystalline coatings. It was experimentally found how effective coatings can be formed and how operation variables effect the surface morphology and the thickness of the coatings. This technology will enlarge the field of applications of crystallization technologies.

References

- [1] J.-W Kim and J. Ulrich, Prediction of degree of deformation and crystallization times of molten droplets in pastillation processes, *I. J. Pharm* **257** (2003), 205–215.
- [2] J.-W. Kim and J. Ulrich, New coating process in pharmaceutical industry by crystallization, *Eng. Life Sci.* **3** (2003), 121–126.

Measurement and analysis of forces during midfacial distraction osteogenesis

W. Knapp^a, Th. Hierl^a, Th. Günter^b and A. Iltschenko^b

^aDepartment of Oral & Maxillofacial Plastic Surgery, University of Leipzig, Leipzig, Germany

^bLeipzig University of Applied Sciences (HTWK), Germany

Tel.: +49 341 9721100; Fax: +49 341 9721109; E-mail: hiet@medizin.uni-leipzig.de

Introduction: Midfacial distraction osteogenesis is a new procedure in the treatment of severe maxillary hypoplasia or retrusion [1,2]. By now, many questions still remain unanswered concerning the time course of the distraction procedure.

Methods: Strain gauges were applied to the distractors of ten patients to measure the forces throughout the whole treatment period. The distractor used was a RED-I/II (Martin Medizintechnik, Tuttlingen, Germany), an extraoral device attached to a halo-frame [1,2]. Strain gauges were fixed to the right and left spindle units as well as to the central rod thus measuring forces for both sides and total force. To collect data continuously over the entire period (up to 3 months), a mobile miniature data logger was developed [3]. Measurements were taken in six second intervals. The data was read out once a week and the patients registered times of meals, adjustments and events on a daily basis.

Results: Absolute amounts and changes of forces could be measured over the entire treatment period. In all patients the course of forces was similar. While initial forces lay between 10–15 N, the maximum forces reached between 40–120 N. During the distraction phase a steady increase in force could be observed (Fig. 1), at the end of which the maximum force was noticed. Subsequently, the forces declined during the retention phase but did not reach the initial level.

Problems in the distraction process occurred in 2 patients where sudden increases in forces correlated with insufficient mobilization during surgery or early osseous fusion. Pain was often seen at force peaks. Temporary reduction of the distraction rate then led to a reduction of pain as well as to a more harmonic course of forces.

Conclusions: The method presented here allowed for the first time to measure forces during midfacial distraction. In this way, distractor activation and individual duration of retention time can be optimized according to the individual biomechanical circumstances.

References

- [1] J.W. Polley and A.A. Figueroa, Rigid external distraction: its application in cleft maxillary deformities, *Plast Reconstr Surg* **102** (1998), 1360–1372.
- [2] T. Hierl, N. Klisch, R. Klöppel and A. Hemprich, Therapie ausgeprägter Mittelgesichtsrücklagen mit Hilfe der Distractionsosteogenese, *MundKieferGesichtsChir* **7** (2003), 7–13.
- [3] Th Hierl, T. Günter, A. Iltchenko, W. Knapp and A. Hemprich, Messung und Aufzeichnung der Kräfte bei der Distractionsosteogenese des Mittelgesicht, *Messtechnische Briefe* **1** (2003), 3–7.

Identification of the mechanical parameters of lungs during expiration

K.J. Palko, M. Kozarski and M. Darowski

Institute of Biocybernetics and Biomedical Engineering, PAS, Warsaw, Poland

Tel.: +48 22 6599143; Fax: +48 22 6597030; E-mail: jpalko@ibib.waw.pl

Introduction: The original method of identification of the basic mechanical parameters of lungs (resistance, compliance) using pressure automatic measurements, combined with time constant measurements, characterised by adding an extra small pneumatic compliance during expiration, is presented in this paper. Insufficiency of respiration usually caused by chronic lung diseases or accidents can be treated by artificial ventilation. In this case, the basic mechanical parameters of lungs (lung/thorax compliance and airways resistance) are often estimated to describe the process of artificial ventilation and also to control the ventilatory treatment for diagnostic and prognostic purposes [2]. The identification of the parameters of lungs is based on an analysis of dynamic signals in the early phase of expiration.

Methods: During automatic measurements of the lungs parameters in the ventilatory support process the influence of spontaneous breath sometimes makes the analysis of obtained results difficult [1,2]. The presented pressure method eliminates this limitation by adding the small pneumatic compliance to the circuit, engaged for the very short time (< 200 ms) at the beginning of expiration when respiratory muscles are non-active.

To determine the compliance of respiratory system a pressure drop is measured, as long as the pressure will correspond to steady states (Fig. 1(a)). To determine the airway resistance time constant RC of the expiratory flow course is used (Fig. 1(b)).

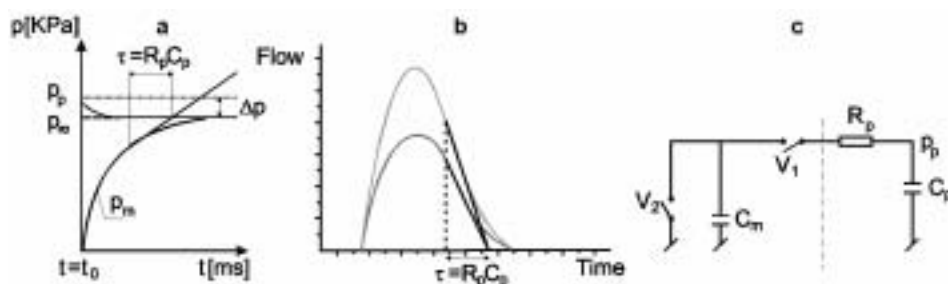


Fig. 1. a. Changes of pressures in the lungs model (p_p) and in the pneumatic compliance C_m (p_m) during measurements, b. Determination of the airway resistance by measurements of the time constant RC of the expiratory flow course c. An electrical analog of the measurement circuit.

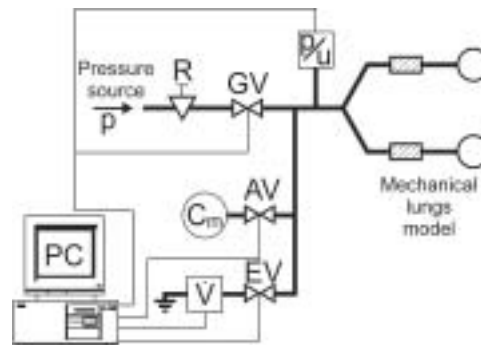


Fig. 2. Measurement circuit for the model investigations. Notations: p/u – pressure-voltage converter p/u , R – pressure regulator, GV – electromagnetic valve, C_m – added compliance, AV – added compliance valve, EV – expiratory valve of respirator, V – flowmeter.

An electrical analog of the applied variant of the added compliance circuit is presented in Fig. 1(c). It includes a linear lungs model represented by compliance C_p and airway resistance R_p . The symbols V_1 and V_2 are added compliance and expiratory valves, respectively. C_m – added compliance.

The measurement circuit is shown in Fig. 2. Pressure p , adjusted on pressure regulator R , is transferred to the electromagnetic valve GV . At the beginning of expiration phase, after time delay τ_1 , the added compliance valve AV opens, and the measurement begins along with registration of pressure Δp by the pressure-voltage converter p/u . After time τ_2 , during which the measurement is done, the expiratory valve EV (of a respirator) opens and it remains opened up to the end of expiration, then both valves AV and EV close. During this time is measured the flow to determine the airway resistance time constant RC of the expiratory flow course. To control the valves and to record the signals, the measuring card and the PC computer system were applied.

The measurements are controlled by computer system using the LabView software. The designed circuit gave possibility of measurement of the pressure drop Δp . The obtained curves were analyzed to determine lungs mechanics. The analysis contained: the time correction of the pressure curve, determination of the pressure drop Δp from linear part of the time characteristic, exponential, straight-line and square approximation parts of curves in order to determine the time constant and determination of the pressure drop Δp at different values of measurement times (200, 300 and 500 ms).

Results: The system was approved on mechanical lungs model. The relative errors of measurements compliance are small (2% for the added compliance of 2 l and 1.5 l), and greater (14% for 0.5 l volume).

Conclusion: The time of measurement about 200 ms is sufficient for the lung compliance determination. Appropriate choice of the added compliance in relation to the lungs compliance is needed.

Acknowledgement: Work financed by State Committee for Science Research (KBN) as grant no. 4 T11E 009 22.

References

- [1] M. Darowski, I. Gottlieb-Inacio, U. Ludwigs and G. Hedenstierna, Assessment of respiratory system compliance by a flow recording method, *Acta Anaesthesiologica Scand* **39** (1995), 462–466.
- [2] M. Darowski, K.J. Palko, A. Jucha and M. Kozarski, Expiratory pressure curve analysis for estimation of lungs mechanics, *Biocybernetics and Biomedical Engineering* **23**(1) (2003), 91–102.

ESB Satellite Symposium: Ultrasound and Bone Biomechanics

Time-frequency representation of transient evoked otoacoustic emission

P. Skorovs

Institute of Biomedical Engineering and Microtechnologies, Riga Technical University, Riga, Latvia
Tel.: +371 7089197; Fax: +371 7089197; E-mail: pskorovs@navigator.lv

Introduction: Transient evoked otoacoustic emissions (TEOAEs) are low level sounds generated by the cochlea in response to transient acoustic stimuli, which can be detected in the outer ear canal by a sensitive microphone [1]. They are essentially present in all normal ears but usually absent or reduced in ears with mild hearing loss. The recording of the TEOAEs has become one of the most important clinical tests of the functionality of the inner ear, but up to now, TEOAEs analysis still relies mostly on a visual inspection of the signal in the time domain. Because of the non-stationary and non-linear nature of the TEOAEs, proper description of the TEOAEs requires simultaneous localization of signal's structures in time and frequency domains.

Within the last decade various new time-frequency analysis methods of the TEOAEs have been proposed; for example, the short-time Fourier transform (STFT), the wavelet transform (WT) as well the Wigner-Ville-based decomposition (WVD) [2–4]. The disadvantages of such methods are well known. Thus, for example, the STFT and the WD suffer from trade-off between the time and frequency resolution. Moreover, one of the basic assumptions in using the STFT and WT is that the signal to be analysed is stationary within a short time window. The main drawback in the practical application of the WVD is that the WVD suffers from cross-terms, which may hide some of the auto-terms.

In the present study, a recently proposed Hilbert-Huang transform (HHT) [5] was used to investigate its advantages and limitations for the time-frequency analysis of the TEOAEs.

Methods and Materials: The HHT [3] combines a method called empirical mode decomposition (EMD) and associated Hilbert spectral analysis.

The EMD decomposes a signal $x(t)$ into a finite and often small number of intrinsic mode functions (IMFs) $imf_i(t)$

$$x(t) = \sum_{i=1}^n imf_i(t) + r(t) \quad (1)$$

where $r(t)$ indicates the residual.

By definition, IMFs have to satisfy two conditions. First, the number of extrema must be equal or differ at most by one from the number of zero-crossings, which is similar to traditional narrow band requirements for the stationary Gaussian process. Second, at any point, the mean value of the envelope, defined by local maxima and the envelope, defined by local minima is zero. The set of the IMFs obtained in this way is unique and specific for the particular time series, since it is based on and derived from the local characteristics of the data. The IMFs could be considered as a more general case of the simple harmonic functions.

In the second, the Hilbert transform is applied to these IMFs. The final presentation of the results is an energy-frequency-time distribution, designated as the Hilbert spectrum.

TEOAE recordings were obtained using ILO288 ECHOPORT system, with a stimulus level of 80 ± 3 dB. The emissions were recorded using the derived non-linear mode for artefact reduction. Each average response consisted of 260 repetitions, sampled at 25,000 Hz. Registration time was 20.48 ms.

To reduce the stimulus artefact, response have been windowed 2.5–20.0 ms post-stimulus time. Signals were band-pass filtered in the range 600–6000 Hz.

A series of computer simulations has been conducted to investigate the performance of the HHT in the time-frequency analysis of the TEOAEs. In the present study, the model proposed by Tognola et al. [4] to simulate TEOAEs of the normal ear was used. According to this model the TEOAEs can be simulated by the summation of the number of gammatones $\gamma_i(t)$

$$x(t) = \sum_{i=1}^n \gamma_i(t) \quad (2)$$

where $\gamma_i(t) = a \cdot t^3 \cdot e^{-2\pi\beta f_i t} \cdot \cos(2\pi f_i t)$, $\beta = 1$ is a constant, $a = (2\pi f_i)^{3.5}$, and f_i is the central frequency (1.0 kHz; 1.5 kHz; 2.2 kHz; 3.3 kHz; and 5.0 kHz) of the gammatone. Custom software was used to analyse the simulated TEOAEs signals by the HHT.

Results and conclusions: The time-frequency representation obtained using the HHT is compared to other time-frequency representations (STFT, WT, and WVD [4]). The results show that the HHT method is superior to other time-frequency representations and gives the most precise definition of particular events in time-frequency space. We can observe very good time-frequency resolution. Each component is well separated, since there are not cross terms. The resolution is definitely higher than obtained by classical time-frequency methods. Using the HHT is easy to extract TEOAEs features.

The HHT is expected to be a useful tool for analysing the TEOAEs in a clinical practice.

References

- [1] R. Probst, B.L. Lonsbury-Martin and G.K. Martin, A review of otoacoustic emissions, *J Acoust Soc Am* **89** (1991), 2027–2067.
- [2] K.J. Blinowska, P.J. Durka, A. Skierski, F. Grandori and G. Tognola, High resolution time-frequency analysis of otoacoustic emissions, *Technol Health Care* **5** (1997), 407–418.
- [3] J. Cheng, Time-frequency analysis of transient evoked otoacoustic emissions via smoothed pseudo Wigner distribution, *Scand Audiol* **24** (1995), 91–96.
- [4] G. Tognola, F. Grandori and P. Ravazzani, Wavelet analysis of click-evoked otoacoustic emissions, *IEEE Trans Biomed Eng* **45** (1998), 686–697.
- [5] N.E. Huang, Z. Shen, S.R. Long, M.C. Wu, H.H. Shih, Q. Zheng, N.-C. Yen, C.C. Tung and H.H. Liu, The empirical mode decomposition and the Hilbert spectrum fro nonlinear and non-stationary time series analysis, *Proc. R. Soc. Lond.* **A454** (1998), 903–995.

The importance of the kidney capsule during trauma

J.G. Snedeker^a, M. Farshad^b, F.R. Schmidlin^c and Niederer^a

^aETH, Zürich, Switzerland

^bEMPA, Dübendorf, Switzerland

^cUniversity Hospital, Geneva, Switzerland

Tel.: +41 1 632 45 87; Fax: +41 1 632 11 93; E-mail: snedeker@biomed.ee.ethz.ch

Introduction: Very little is known about either the material properties of the renal capsule or its mechanical influence during renal trauma. This study includes two phases: the determination of dynamic

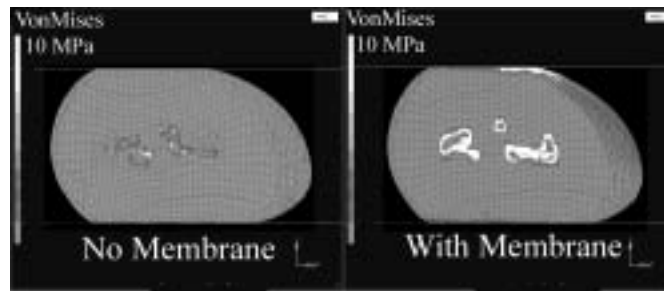


Fig. 1. Stiffness and breaking stress heavily depend on deformation rate.

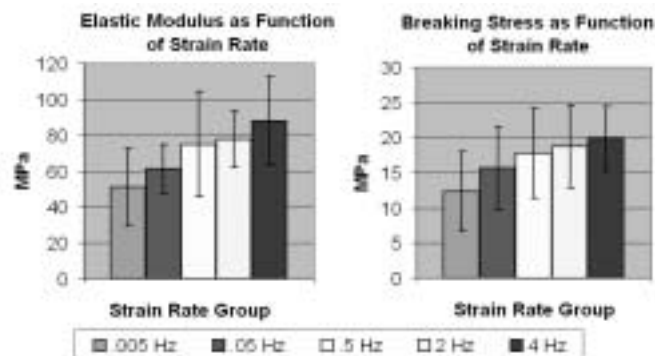


Fig. 2. There is very good agreement between experimental data and the mathematical model.

material properties of the kidney capsule, and the implementation of a mathematical material model into a finite element simulation of renal trauma.

Methods: Uniaxial tensile tests were performed on adult pig kidneys within 36 hours of animal euthanization. Samples were delicately excised using a sheet metal template to yield symmetric samples. After the test protocol was validated for repeatability, test samples with a nominal length of 20 mm were tested at constant stretch rates of 0.005, 0.05, 0.5, 2.0, and 4.0 Hz.

In order to incorporate viscoelastic properties of the renal capsule into a finite element model of the kidney, a mathematical, large-strain, incompressible, first order Ogden hyper/viscoelastic model was developed for the capsule. The hyperelastic Ogden coefficients and Prony series viscoelastic coefficients were determined using an iterative curve fitting approach. See [1] for theoretical details underlying this constitutive law.

Finally, the capsule was included within a detailed finite element model of the human kidney that had been developed for use in for trauma research [2]. The kidney model is based upon the the NIH Visible Human Female dataset, and employs viscoelastic materials to successfully simulate the dynamic behavior of the cortex and mudula. The kidney model (both with and without the capsule) was subjected to simulated parallel plate uniaxial compression at 5 m/s. The effect of the capsule inclusion on the resulting stress patterns was analyzed.

Results: As expected, the mechanical properties of the capsular membrane are dependent on the rate of strain; It becomes stiffer with increasing deformation. While breaking stress was also observed to depend on the rate of deformation, breaking strain appeared to be independent of strain rate. The relationship between the elastic modulus, breaking stress and strain rate is readily apparent in Fig. 1. The required

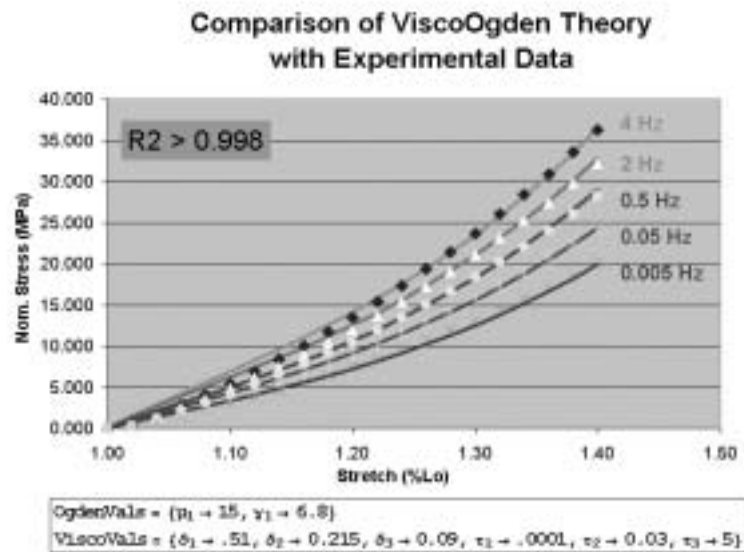


Fig. 3. The capsular membrane increases stress magnitude at interior renal surfaces.

coefficients for a first order Ogden visco-hyperelastic constitutive equation with three characteristic relaxation frequencies are shown in Fig. 2. Also illustrated is the quality of fit between the mathematical material model, the FE implemented theory, and experimental data (Fig. 3).

In whole kidney compression, the addition of the renal capsule resulted in a five fold increase of internal stress magnitude within the paranchymal tissues of the cortex and medulla. The highest stress concentrations were located at the highly convoluted interior surfaces of the kidney.

Discussion/conclusions: Dynamic testing of the porcine renal capsule reveals a heavy material property dependence on deformation rate. The fact that the inclusion of the rate dependent renal capsule to the three dimensional kidney model drastically increases the predicted stress levels during traumatic loading implies that the capsule, which functions primarily as an aid to blood filtration, may actually increase the risk of tissue damage during high-speed abdominal trauma. However, this finding conflicts with accident statistics and practical medical experience, in which kidneys exposed to traumatic load are most likely to rupture at flawed regions of the renal capsule [3]. This apparent contradiction warrants further investigation.

References

- [1] J.C. Simo and T.J.R. Hughes, *Computational Inelasticity*, Springer, New York, New York, 1998.
- [2] J.G. Snedeker, M. Bajka, J.M. Hug, G. Székely and P. Niederer, The creation of a high-fidelity finite element model of the kidney for use in trauma research, *J. Vis. Comp. Anim.* **13** (2002), 53–64.
- [3] F.R. Schmidlin, P. Schmid, T. Kurtyka, C.E. Iselin and P. Graber, Force Transmission and Stress Distribution in a computer simulated model of the kidney: an analysis of the injury mechanisms in renal trauma, *J. Trauma* **40** (1996), 791–796.

Experimental and numerical study on mechanoregulation of tissue differentiation around a loaded implant in a bone chamber

H. Van Oosterwyck^a, L. Geris^a, J. Duyck^b, M. De Cooman^c, A. Andreykiv^d, F. van Keulen^d, R. Puers^c, I. Naert^b and J. Vander Sloten^a

^aK.U. Leuven, Division of Biomechanics and Engineering Design, Belgium

^bK.U. Leuven, Division of Prosthetic Dentistry, Belgium

^cK.U. Leuven, Division ESAT-MICAS, Belgium

^dDelft University of Technology, Faculty of Design, Engineering and Production, The Netherlands

Tel: +32-16-327067, Fax: +32-16-327994, E-mail: hans.vanoosterwyck@mech.kuleuven.ac.be

Introduction: It is well known that mechanical loading can interfere with tissue differentiation processes, as encountered during bone fracture healing. Similar interactions can be expected for bone healing around immediately loaded endosseous implants, as e.g. demonstrated in the dog experiments of Søballe and co-workers [1]. Mechanical loading may enhance bone formation, and in this way, mechanical factors may be important for bone engineering applications. To fully exploit the potential beneficial role of mechanical loading in bone engineering, a profound understanding of the mechanoregulation of tissue differentiation is needed. A combined experimental and numerical approach was followed here to study tissue differentiation around an implant in a well-controlled mechanical environment.

Materials and methods: A bone chamber was designed that was implanted in the tibia of New Zealand white rabbits. Perforations in the chamber walls allowed tissue ingrowth in the chamber. Central to the chamber a cylindrical implant is placed that can be axially loaded. The chamber consists of an outer chamber, which remains integrated in the host bone tissue during the entire experiment, and an inner chamber, which can be harvested without having to sacrifice the animal. This enables to perform several experiments under different mechanical (or other) conditions within the same animal.

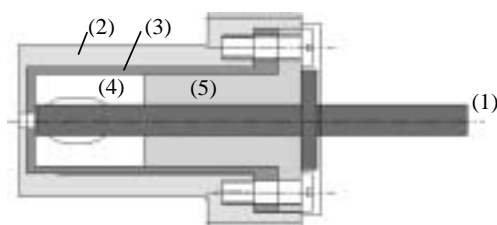


Fig. 1. Schematic drawing of the repeated sampling bone chamber: (1) implant; (2) outer chamber; (3) inner chamber; (4) tissue; (5) teflon bearing.

Preliminary loading experiments were performed, consisting of a cyclic axial displacement of $50 \mu\text{m}$ (800 cycles/day, 2 days/week).

Numerical simulations of tissue ingrowth and differentiation were carried out as well, and compared to histological sections. A model, originally developed by Prendergast [2] and Huiskes [3], was applied here to mathematically describe the mechanoregulation of skeletal tissue differentiation. The model makes use of a biphasic description of the elastic behaviour of the differentiating tissues and defines the mechanical stimulus for tissue differentiation in terms of relative fluid flow and octahedral shear strain. Depending on the values of the stimulus, mesenchymal stem cells were allowed to differentiate into either fibroblasts, chondrocytes or osteoblasts. Biphasic finite element models of the tissues inside the

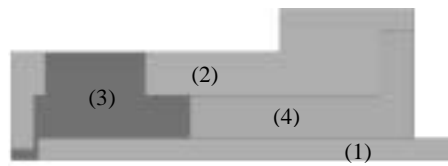


Fig. 2. Material distribution in an axisymmetric FE model of the bone chamber: (1) implant; (2) chamber walls; (3) tissue; (4) teflon bearing.

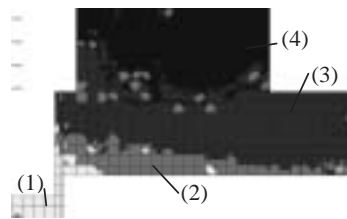


Fig. 3. Simulated tissue distribution in bone chamber, according to mechanoregulatory model, for 50 μm implant displacement: (1) fibrous tissue; (2) cartilage; (3) immature bone; (4) mature bone.

chamber were used to calculate the mechanical stimulus distribution. The model also takes into account mesenchymal cell migration, which was mathematically described by means of a diffusion equation [4].

Results and discussion: First histological results showed more bone ingrowth for loaded test samples than for unloaded controls after 4 weeks. Simulation results were in good qualitative agreement with the histological findings. Considerable amounts of (trabecular) bone tissue were found in the chamber, but near the implant interface more fibrous and cartilaginous tissue were predicted, primarily because of the higher shear strains encountered here. Although these results are promising with respect to the validity of the model, more experiments with different loading parameters will have to be conducted in order to fully validate the model in a more quantitative way.

References

- [1] K. Søballe et al., Tissue ingrowth into titanium and hydroxyapatite-coated implants during stable and unstable mechanical conditions, *Journal of Orthopaedic Research* **10** (1992), 285–299.
- [2] P.J. Prendergast et al., Biophysical stimuli on cells during tissue differentiation at implant interfaces, *Journal of Biomechanics* **30** (1997), 539–548.
- [3] R. Huiskes et al., A biomechanical regulatory model for periprosthetic fibrous-tissue differentiation, *Journal of Materials Science: Materials in Medicine* **8** (1997), 785–788.
- [4] D. Lacroix et al., Biomechanical model to simulate tissue differentiation and bone regeneration: application to fracture healing, *Medical and Biological Engineering and Computing* **40** (2002), 14–21.